

1 **Synthesis of in situ marine calcium carbonate**
2 **dissolution kinetic measurements in the water column**

3 **Ben A. Cala^{1,2}, Olivier Sulpis³, Mariette Wolthers², and Matthew P.**
4 **Humphreys¹**

5 ¹NIOZ Royal Netherlands Institute for Sea Research, Department of Ocean Systems (OCS), Texel, The
6 Netherlands

7 ²Utrecht University, Department of Earth Sciences, Princetonlaan 8A, 3584 CB Utrecht, The Netherlands

8 ³CEREGE, Aix Marseille Univ, CNRS, IRD, INRAE, Aix-en-Provence, France

9 **Key Points:**

- 10 • Published in situ carbonate mineral dissolution rate measurements in the water
11 column are compiled and the saturation state (Ω) is estimated.
- 12 • Dissolution rates differ by 2 orders of magnitude at the same Ω , mainly due to dif-
13 ferences in experimental design between the studies.
- 14 • The compiled dataset is used to investigate dissolution above the saturation hori-
15 zon and to validate laboratory observations.

Corresponding author: Ben A. Cala, ben.cala@nioz.nl

16 **Abstract**

17 Calcium carbonate (CaCO_3) dissolution is an integral part of the ocean's carbon
 18 cycle. However, laboratory measurements and ocean alkalinity budgets disagree on the
 19 rate and loci of dissolution. In situ dissolution studies can help to bridge this gap, but
 20 so far published studies have not been utilised as a whole because they have not previ-
 21 ously been compiled into one dataset and lack carbonate system data to compare be-
 22 tween studies. Here, we compile all published measurements of CaCO_3 dissolution rates
 23 in the water column (11 studies, 752 data points). Combining World Ocean Atlas data
 24 (temperature, salinity) with the neural network CANYON-B (carbonate system variables),
 25 we estimate seawater saturation state (Ω) for each rate measurement. We find that dis-
 26 solution rates at the same Ω vary by 2 orders of magnitude. Using a machine learning
 27 approach, we show that while Ω is the main driver of dissolution rate, most variability
 28 can be attributed to differences in experimental design, above all bias due to (diffusive)
 29 transport and the synthetic or biogenic nature of CaCO_3 . The compiled dataset supports
 30 previous findings of a change in the mechanism driving dissolution at $\Omega_{\text{crit}} = 0.8$ that
 31 separates two distinct dissolution regimes: $r_{\text{slow}} = 0.29 \cdot (1 - \Omega)^{0.76}$ mass% day⁻¹ and
 32 $r_{\text{fast}} = 2.95 \cdot (1 - \Omega)^{2.29}$ mass% day⁻¹. Above the saturation horizon, one study shows
 33 significant dissolution that cannot solely be explained by established theories such as zoo-
 34 plankton grazing and organic matter degradation. This suggests that other, non-biological
 35 factors control shallow dissolution.

36 **1 Introduction**

37 Marine carbonate minerals such as calcium carbonate (CaCO_3) play an integral
 38 role in the Earth's carbon cycle, regulating the oceanic uptake of CO_2 and acting as a
 39 buffer against ocean acidification (Zeebe & Wolf-Gladrow, 2001; Archer et al., 2009). The
 40 increase of atmospheric CO_2 lowers the ocean's pH, which enhances the dissolution of
 41 carbonate minerals, increasing the ocean's alkalinity. The depth of CaCO_3 dissolution
 42 influences the timescale on which the ocean can mitigate the drastic increase in anthro-
 43 pogenic CO_2 : regeneration of alkalinity in the shallow ocean affects atmospheric CO_2
 44 more immediately than in the deep sea, from where the regenerated alkalinity first needs
 45 to be transported into surface waters.

46 Despite its importance, marine CaCO_3 production and dissolution are still poorly
 47 constrained (Liang et al., 2023). Marine CaCO_3 most commonly occurs in the forms of
 48 calcite (e.g., foraminifera and coccolithophores) and aragonite (e.g., pteropods). While
 49 most studies focus on calcite, there is growing evidence that the more soluble aragonite
 50 makes a major contribution to CaCO_3 cycling, with aragonite estimated to contribute
 51 over 20% to particulate inorganic carbon (PIC) flux (Buitenhuis et al., 2019; Neuker-
 52 mans et al., 2023). The magnesium-rich form of calcite (high-Mg calcite), produced by
 53 some foraminifera, algae and teleosts, has also been proposed to play an important role
 54 (Wilson et al., 2009; Woosley et al., 2012), but its contribution remains unquantified.

55 Additionally, seawater alkalinity measurements provide evidence that the major-
 56 ity of CaCO_3 dissolution occurs in shallow waters (Feely et al., 2002; Sulpis et al., 2021)
 57 that are supersaturated with respect to both calcite and aragonite and therefore in the-
 58 ory dissolution should not occur. Specifically, biogeochemical budgets reveal an excess
 59 of alkalinity in these waters that can only be explained by carbonate mineral dissolution.
 60 Although this phenomenon has been known for decades (Milliman et al., 1999), a con-
 61 vincing explanation for apparent dissolution above the saturation horizon ($\Omega > 1$) re-
 62 mains elusive.

63 The dissolution rate depends on the water’s saturation state (Ω) for each mineral:

$$64 \quad \Omega = \frac{[\text{Ca}^{2+}][\text{CO}_3^{2-}]}{K_{\text{sp}}^*} \quad (1)$$

65 where square brackets indicate the concentration of the enclosed species and with the
 66 solubility product

$$67 \quad K_{\text{sp}}^* = [\text{Ca}^{2+}]_{\text{sat}}[\text{CO}_3^{2-}]_{\text{sat}}, \quad (2)$$

68 a function of temperature (T), salinity (S), and pressure which is different for each min-
 69 eral. The kinetics of carbonate mineral dissolution with respect to Ω have mainly been
 70 assessed in laboratory settings (Morse & Berner, 1972; Keir, 1980; Gehlen et al., 2005;
 71 Subhas et al., 2015; Naviaux, Subhas, Rollins, et al., 2019), although more recently in
 72 situ measurements have also been used (Dong et al., 2019; Naviaux, Subhas, Dong, et
 73 al., 2019; Subhas et al., 2022). Measured dissolution rates (r) are canonically fitted to
 74 the function

$$75 \quad r = k(1 - \Omega)^n \quad (3)$$

76 where k is the rate constant and n is the pseudo reaction order (Morse & Arvidson, 2002).
 77 Since K_{sp}^* increases with higher pressure and lower temperature (Hawley & Pytkowicz,

1969; Mucci, 1983), Ω decreases with depth and the highest dissolution rate is therefore expected in the deep ocean.

Peterson (1966) and Berger (1967) found that dissolution of calcite particles attached to a mooring in the Pacific started high in the water column but increased only slightly with depth until approximately 4000 m, where dissolution suddenly began to increase rapidly. This was first explained through hydrodynamic influences such as current velocity (Edmond, 1974), but because this effect could also be observed in the laboratory (Morse & Berner, 1972; Keir, 1980), a change in reaction kinetics at the surface of the carbonate minerals at critical undersaturation soon became more a more accepted explanation (Milliman, 1977). While Teng (2004) observed three distinct dissolution mechanisms, from step edge retreat, through defect-assisted edge pit formation to homogeneous edge pit formation with increasing undersaturation, Naviaux, Subhas, Rollins, et al. (2019) found that at the relevant temperatures in seawater, the mechanism directly switches from step edge retreat to homogeneous etch pit formation at a critical saturation state $\Omega_{\text{crit}} \approx 0.75$. For $\Omega_{\text{crit}} < \Omega < 1$, dissolution is slower and less sensitive to the saturation state and for $\Omega < \Omega_{\text{crit}}$ dissolution increases more rapidly with undersaturation. When $\Omega > 1$, seawater is oversaturated, so no dissolution should occur.

One issue with applying laboratory results to the real ocean is environmental complexity. While laboratory experiments happen in known and controlled environments, the ocean is complex with many (often biological) processes happening simultaneously under wide ranges of variable hydrographic conditions that cannot be comprehensively simulated in the laboratory. In situ measurements of dissolution rates (Table 1) could help to bridge the gap between laboratory experiments and oceanographic alkalinity data by implicitly including the effects of these processes and background variability, also helping to validate and inform future laboratory studies.

Fewer than a dozen studies with in situ dissolution rate measurements have been conducted (Table 1). Due to the variety in the experimental design (Figure 1) and the rates being reported in mutually incompatible units, it is challenging to compare the results of in situ studies with each other and thus draw overall conclusions about real-world dissolution. Furthermore, much of the data in older publications is only presented in the form of depth-rate plots, with other variables describing the water chemistry (DIC, TA, pH and Ω) and environment (salinity, temperature and dissolved oxygen) around the sam-

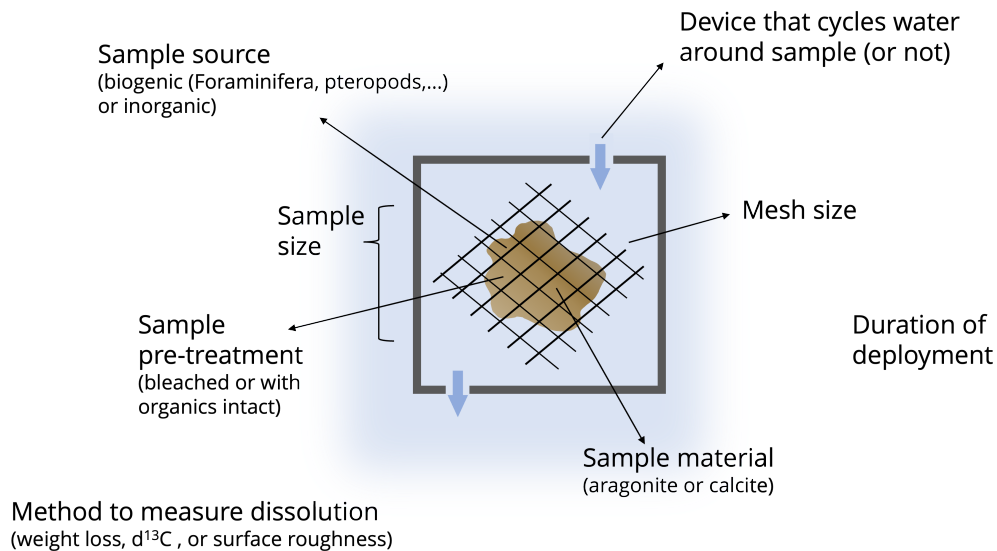


Figure 1. Overview of how experimental design can vary between the different studies for in situ dissolution measurements. Half of the categories describe the setup of the experiment: the duration of the samples' deployment in the water column, whether a device was employed to cycle water around the sample to avoid stagnation effects, and what method was used to determine how much dissolution took place. Mesh size refers to the size of the openings in the fine mesh the sample was placed into during deployment. The other categories describe the sample itself. The sample source refers to whether the sample was inorganic (e.g., calcite crystal) or biogenic (e.g., the shell of a pteropod). Sample pre-treatment refers to the oxidative cleaning which some experiments conducted on the biogenic samples to remove any organic coatings that might have still been intact. The material is either aragonite (e.g., pteropods) or calcite (e.g., foraminifera). The size of the sample refers to the diameter of one unit/grain of the sample.

110 ple either not recorded or not included. Therefore, the results of these in situ studies have
111 mostly been considered individually and not systematically examined as a whole.

112 Here, we present a new compilation of (to the best of our knowledge) all published
113 in situ marine carbonate dissolution measurements in the water column. For each mea-
114 surement, we have estimated the set of hydrographic variables required to investigate
115 dissolution (temperature, salinity (S), dissolved oxygen, pH_T , total alkalinity (TA), dis-
116 solved inorganic carbon (DIC), and the saturation state of calcite (Ω_{ca}) and aragonite
117 (Ω_{ar}) using the World Ocean Atlas 2018 (WOA18) dataset together with the neural net-
118 work CANYON-B (Bittig et al., 2018). We used a machine learning (ML) regression model

119 to understand how much of the variability in the measured dissolution rate can be ex-
120 plained by each aspect of the experimental design (Figure 1) and in what way each as-
121 pect affects the dissolution rate. We use the compiled dataset to assess whether signif-
122 icant dissolution above the saturation horizon has been observed by in situ studies. Ad-
123 ditionally, we validate laboratory measurements of different dissolution regimes based
124 on the degree of undersaturation.

125 **2 Methods**

126 **2.1 Data compilation**

127 First, the dissolution rates from the various in situ studies (Table 1) were compiled.
128 To find suitable studies, we used various combinations of the keywords ‘dissolution rate’
129 ‘calcite’, ‘aragonite’, ‘foraminifera’, ‘marine’, ‘ocean’, ‘in situ’, ‘mooring’, and ‘measure-
130 ment’ (e.g., ‘dissolution rate calcite in situ’) in Google Scholar and Semantic Scholar. Since
131 we focused on dissolution in the water column, we did not consider studies that deter-
132 mine dissolution rates from sediment cores (e.g., porewater measurements) or at the sediment-
133 water interface. We also excluded studies that estimate dissolution rates from sediment
134 trap samples. Beside the initial keyword-based searches, we identified additional stud-
135 ies by reviewing the references cited within the already selected papers. In studies where
136 the dissolution rates were only reported in a figure instead of being tabulated, the data
137 were extracted using WebPlotDigitizer (Rohatgi, 2021).

138 Where available, additional information such as percentage fragmentation of the
139 sample (T81, M82), measurement uncertainty (P66, D19, N19, S22) and environmen-
140 tal variables (D19, N19, S22) were also retrieved, along with complementary informa-
141 tion about the sample (material, biogenic, organic coating), experimental setup (water
142 cycling device, particle size, mesh size), and measurement technique (for an overview in
143 the differences of experimental design see Figure 1). As described in the accompanying
144 paper (Metzler et al., 1982), the measurements from Station 2 in M82 were of low qual-
145 ity due to mechanical loss of the sample and are therefore not included in this compi-
146 lation.

Table 1. Overview of the methods of all published studies measuring CaCO_3 dissolution rates in situ in the water column. ‘*Cleaned?*’ refers to whether the sample underwent an oxidative cleaning protocol to remove organic coatings.

| Source | Abbrev. | Location | Duration | Cycling device? | Rate determination | Mesh size (μm) | Sample | Biogenic? | Cleaned? | Sample size |
|------------------------|-------------------|--|-----------------------|---------------------------------------|----------------------------|-----------------------------|--|--|---|---|
| Peterson (1966) | P66 | 19N, 169W | 4 months | no | weight loss | – | Calcite crystal | no | – | cm-sized |
| Berger (1967) | B67 | 19N, 169W | 4 months | no | weight loss | 62 | Foraminifera assemblage Foraminifera assemblage | yes yes | yes no | unknown unknown |
| Milliman (1977) | M77 | 23N, 70W 23N, 65W 23N, 55W 26N, 60W | 4 months, 9 months | no | weight loss | 20-40 | Foraminifera (O universa, G sacculifer) Aragonite ooids Mg Calcite ooids (12% Mg) | yes no no | no – – | 250-500 μm (L) |
| Honjo and Erez (1978) | HE78 | 32N, 155W | 79 days | yes (0.6 mL/min) | weight loss | 0.4-0.6 | Reagent calcite Large calcite crystal Synthetic aragonite Foraminifera assemblage Foraminifera assemblage G sacculifer G bulloides G pachyderma E huxleyi C neohelis Pteropod assemblage | no no no yes yes yes no no yes yes yes no | – – – yes yes no no no yes yes no | 10-53 μm (XXS) 0.7-1 μm (XXL) 10-53 μm (XXS) 63-1000 μm 63-1000 μm >250 μm (L) >250 μm (L) >149 μm (M) XXXS XXXS XXXS >831 μm (XXL) |
| Thunell et al. (1981) | T81 | 4N, 82W | 123 days | no | weight loss, fragmentation | 100 | Foraminifera assemblage | yes | no | >250 μm (L) |
| Metzler et al. (1982) | M82 | 0N, 152W | 123 days | no | weight loss, fragmentation | 44 | Foraminifera assemblage | yes | yes | 62-125 μm (XS) 125-177 μm (S) 177-250 μm (M) 250-420 μm (L) >420 μm (XL) |
| Troy et al. (1997) | T97 | 23N, 158W | 3 days | no | Surface roughness | 333 | Calcite crystal | no | – | cm-sized |
| Fukuhara et al. (2008) | F08 | 30N, 175E | 23 days | most not, only at 2 depths (5 mL/min) | weight loss | most 63, some 30 | Aragonite crystal Calcite crystal G sacculifer G inflata G truncatulinoides | no no yes yes yes | – – no no no | 3 size fractions: 125-250 μm (S) 250-425 μm (L) 425-500 μm (XL) |
| CDIsK-IV | D19 N19 S22 | 28N, 155W 35N, 151W 42N, 148W 50N, 145W | 24 - 58 h | yes (5 mL/min) | d13C | 8 8 0.8 | Synthetic Aragonite Synthetic Calcite E huxleyi | no no yes | – – yes | 250-495 μm (L) 20-53 μm (XXS) XXXS |

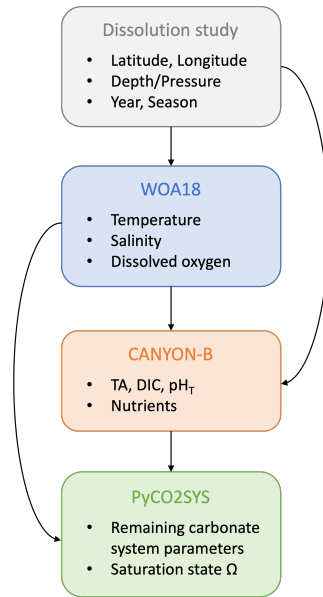


Figure 2. Summary of the workflow to estimate Ω . Starting from the top (Dissolution study), each box represents a workflow step in which the outputs listed inside the box were obtained. The arrows show where outputs from a step were used as inputs to a later step.

147

2.2 Estimation of Ω

148

149

150

151

152

153

In most cases, the dissolution rate was reported as a function of depth but with carbonate system variables for the surrounding seawater either not measured or not recorded, making it impossible to directly calculate the seawater saturation state. Instead, we developed a method to estimate Ω using the World Ocean Atlas 2018 (WOA18) and the neural network CANYON-B (Bittig et al., 2018) (Figure 2). The validation of this method is described in the SI.

154

155

156

157

158

159

160

Temperature (Locarnini et al., 2018), salinity (Zweng et al., 2019), and dissolved oxygen data (Garcia et al., 2019) were taken from WOA18. For the upper 57 levels (1500 m) we took the seasonal statistics and below that the annual averages of the objectively analysed climatology (standard depth levels (102 levels, 0-5500 m) at 1° resolution, using data from all available years ('all' or 'decav' datasets)). The data at the grid point closest to the measurement site were interpolated over depth and appended to the compiled data.

161

162

This environmental data, as well as the geographic location and time of the expedition (for experiments lasting several months, we used the mid-point of the experiment),

163 were used as input parameters for CANYON-B (Bittig et al., 2018). CANYON-B is a
164 Bayesian neural network trained on the GLODAPv2 dataset (Olsen et al., 2016) that
165 calculates marine carbonate system variables (TA, DIC, pH) and nutrients (phosphate,
166 silicate, nitrate) as a function of geographic location, time (month and year), depth, pres-
167 sure, temperature, salinity, and dissolved oxygen.

168 Using the DIC-pH_T pair as inputs, the remainder of the carbonate system, includ-
169 ing Ω , was calculated with PyCO2SYS (version 1.8.1) (Humphreys et al., 2022) with the
170 carbonic acid dissociation constants K_1 and K_2 of Sulpis et al. (2020), the borate:chlorinity
171 of Uppström (1974), the K_{HSO_4} of Dickson (1990), and the calcite and aragonite K_{sp} of
172 Mucci (1983) together with the PyCO2SYS defaults for the other optional constants.

173 The only studies that reported hydrographic variables with their dissolution ex-
174 periments were during the CDisK-IV cruise, which includes N19, D19, and S22. A com-
175 parison between CDisK-IV measurements (Berelson et al., 2022) and the values gener-
176 ated by our method described above can be found in the SI (Figure S9 and S10). In this
177 study and our final data compilation, we report their measured values alongside our es-
178 timates for the other studies.

179 **2.3 Uncertainty propagation**

180 The uncertainty of Ω was estimated by propagating the uncertainties for each of
181 the variables needed for its determination through each of the workflow steps (Figure
182 2).

183 The uncertainty associated with the variables obtained from WOA18 is represented
184 by their standard deviation. We used the objectively analysed climatology, which does
185 not include a standard deviation. Therefore, we rely on the standard deviation of the
186 statistical mean of the measurements that were made at that grid point at a certain stan-
187 dard depth level. We only considered standard deviations that were determined with enough
188 measurements (>4) to yield a meaningful value.

189 For temperature and salinity, the standard deviation was calculated from a com-
190 bination of seasonal data for the upper 1500 m of the water column and annual data for
191 the remaining depths. However, where the seasonal dataset contained fewer than 5 mea-
192 surements at any given depth, we used the annual mean for the entire water column. For

193 dissolved oxygen, the number of measurements available was much lower, resulting in
 194 no valid standard deviations for most grid cells. In this case, we calculated the average
 195 of all standard deviations at grid points that had at least 5 measurements shallower than
 196 1500 m within a 10-degree radius around the experiment site. For all variables, if fewer
 197 than 5 measurements existed at deeper depth levels, the closest shallower valid standard
 198 deviation was used. Subsequently, the standard deviations were interpolated across depth
 199 and appended to the compiled dataset.

200 The 90th percentile for the estimated uncertainty of TA, DIC, pH and nutrients
 201 inherent to CANYON-B, $\sigma_{\text{CANYON-B}}^2(m)$ is given by Bittig et al. (2018). We combined
 202 this with the uncertainty stemming from WOA18 from temperature (T), salinity (S),
 203 and dissolved oxygen ($[\text{O}_2]$):

$$204 \quad \sigma(m) = \sqrt{\left(\frac{\partial m(T)}{\partial T}\right)^2 \sigma^2(T) + \left(\frac{\partial m(S)}{\partial S}\right)^2 \sigma^2(S) + \left(\frac{\partial m([\text{O}_2])}{\partial [\text{O}_2]}\right)^2 \sigma^2([\text{O}_2]) + \sigma_{\text{CANYON-B}}^2(m)} \quad (4)$$

205 The derivatives $\frac{\partial m(x)}{\partial x}$ were calculated by finite forward difference, with

$$206 \quad \frac{\partial m(x)}{\partial x} = \frac{m(x + \Delta x) - m(x)}{\Delta x} \quad (5)$$

207 for which CANYON-B was run again with $x + \Delta x$. We chose $\Delta T = 0.001$ °C, $\Delta S =$
 208 0.001 , and $\Delta[\text{O}_2] = 0.001$ $\mu\text{mol kg}^{-1}$ but the results were stable with Δx an order of
 209 magnitude larger or smaller.

210 We propagated the uncertainties in TA, DIC, temperature, salinity and nutrients
 211 through to Ω using the in-built uncertainty propagation tool in PyCO2SYS. In this step,
 212 we also included uncertainty stemming from the equilibrium constants of the carbonate
 213 system and the solubility products of calcite and aragonite, as implemented in PyCO2SYS
 214 following Orr et al. (2018). However, by default PyCO2SYS propagates uncertainties as-
 215 suming that the uncertainty in each argument is independent, which is not the case here:
 216 for instance, temperature is used to calculate DIC and pH in CANYON-B, so their un-
 217 certainties will covary. However, this covariance has a negligible contribution to the over-
 218 all uncertainty in CANYON-B outputs because the majority of their uncertainty arises
 219 from the inherent uncertainty in the CANYON-B model, rather than propagated uncer-
 220 tainties in its input variables, and is thus independent of the input uncertainties.

2.4 Feature importance

To evaluate the contribution of different features of the experimental design to the measured dissolution rate, we used a supervised machine learning model to predict the dissolution rates of mass-normalised measurements.

The independent variables (predictors) were Ω and seven features describing the experimental design (Table 1 and Figure 1): (1) size fraction of the CaCO_3 samples (in eight categories, from XXXS to XXL; Table S1), (2) mesh size, (3) whether the particle was inorganic or biogenic and whether it underwent an oxidative cleaning protocol to remove organic coatings, (4) if a water cycling device was used to avoid diffusion effects, (5) the deployment time of the CaCO_3 sample, (6) mineral form (calcite or aragonite), and (7) the measurement method (weight loss or $\delta^{13}\text{C}$). Dissolution measurements with missing data for any one of these predictors were excluded from the model.

A predictive regression model was implemented with the XGBoost (Extreme Gradient Boosting) library (version 1.7.1) (Chen & Guestrin, 2016). The XGBoost regressor is an ensemble machine learning model which is made up of multiple decision trees. A decision tree is a hierarchical model where data is continuously split based on a feature at a decision node, until finally reaching one of the leaf nodes that represent the possible outcomes of the model (Breiman et al., 1984). XGBoost utilizes a gradient boosting framework, where new trees are gradually added to the ensemble in such a way that the loss gradient (difference between predicted and actual outcome) is minimised. This approach is especially suited for capturing non-linear relationships and interactions between features.

The dataset was randomly split into training and testing sets with a ratio of 80:20. To maximise model performance and avoid overfitting, the model parameters need to be tuned, for which the training set was further randomly split into five folds for cross-validation. A grid search was performed using the GridSearchCV function from the scikit-learn library (version 1.2.2) (Pedregosa et al., 2011) with R-squared (R^2) as the scoring metric. Afterwards, the XGBoost Regressor was trained on the entire training set with squared error as the learning objective using the optimal parameters (see SI) obtained in the previous step. The trained model was then evaluated on the testing set using R^2 , the mean absolute error (MAE) and mean squared error (MSE) or root mean squared error (RMSE). For all steps (hyperparameter tuning, model training and evaluation) the

253 data were weighted such that the total weight of each study was equal so that studies
 254 with a greater number of measurements did not have a greater influence on the model.
 255 Without this weighting, the differences between the data points of one study with many
 256 data points would overshadow the variations between different studies. Categorical data
 257 were encoded by mapping each unique label to an integer value.

258 Machine learning models are often regarded as ‘black boxes’. Since their decision-
 259 making process is complicated with various layers, it is difficult to understand how the
 260 model arrives at certain predictions (Breiman, 2001b; Molnar, 2022). Two methods were
 261 employed here to gain insight into the importance and relationship of a specific feature
 262 to the model’s prediction of dissolution rates: Permutation Feature Importance (PFI)
 263 (Breiman, 2001a) and Partial Dependence Plots (PDPs) (Friedman, 2001). For both, we
 264 used the implementation in the scikit-learn library (version 1.2.2). PFI randomly per-
 265 mutates the values of each feature and measures how much this decreases the model’s
 266 performance. It gives insight into how relevant a feature is for the model to arrive at a
 267 correct prediction. PFI was calculated for the test data using mean squared error (MSE)
 268 as the scoring metric. PDPs show how changing a certain feature affects the model out-
 269 put by showing the relationship between each feature and the model’s predictions while
 270 holding all other features constant. Thus, PDPs can also be used to identify non-linear
 271 relationships between features and the model’s prediction.

272 **2.5 Investigating dissolution regimes**

273 When determining the reaction kinetics for dissolution, equation 3 is linearised to

$$274 \log_{10} r = \log_{10} k + n \cdot \log_{10}(1 - \Omega) \quad (6)$$

275 With two dissolution regimes, the data must to be fitted to two linear functions
 276 of the form of equation 6 which intercept at Ω_{crit} . If no prior assumption of Ω_{crit} is made,
 277 a single function combining the two linear regimes with a flexible intercept is needed.

278 To this end, we used the error function

$$279 \text{erf}(x) = \frac{2}{\sqrt{\pi}} \int_0^x e^{-t^2} dt \quad (7)$$

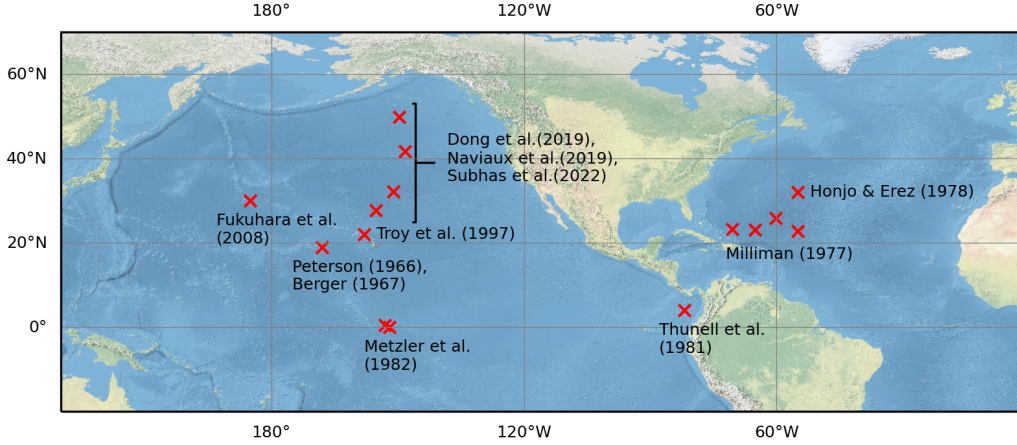


Figure 3. Locations of in situ dissolution rate measurements.

280 multiplied by two linear functions of the form $f(x) = ax + b$ to get

$$\begin{aligned}
 y &= (0.5 \cdot (+\operatorname{erf}(p \cdot (x + x_{intcp})) + 1) \cdot (a_2x + b_2)) \\
 &+ (0.5 \cdot (-\operatorname{erf}(p \cdot (x + x_{intcp})) + 1) \cdot (a_1x + b_1))
 \end{aligned}
 \tag{8}$$

282 where $y \equiv (\log_{10} r)$, $b \equiv (\log_{10} k)$, $a \equiv n$, and $x \equiv \log_{10}(1 - \Omega)$ from equation 6.
 283 $x_{intcp} = \frac{b_1 - b_2}{a_2 - a_1}$ is the intercept of the two linear functions, which is Ω_{crit} , and p is a term
 284 that determines how rounded the corner is where the two linear functions meet (here:
 285 $p = 80$). f_1 represents the slower dissolution regime for $\Omega_{crit} < \Omega < 1$ and f_2 the faster
 286 one for $\Omega < \Omega_{crit}$.

287 The fitting of the data points is achieved with SciPy’s least_squares function (SciPy
 288 version 1.7.3 (Virtanen et al., 2020)) using initial guesses of $n_1 = 0$, $n_2 = -1.5$, $\log_{10} k_1 =$
 289 -3.5 , and $\log_{10} k_2 = -1.5$.

290 **3 Results and discussion**

291 **3.1 Description of compiled in situ measurements**

292 The compiled dataset consists of 752 data points. The experiments used diverse
 293 sets of samples, such as deep-sea sediments made up of foraminiferal assemblages, syn-
 294 thetic calcite crystals, coccolithophores, pteropods, or high-Mg calcite ooids. Nonethe-
 295 less, only a fifth of the samples consist of aragonite and less than half are of biogenic ori-
 296 gin. All measurements were made in the northern hemisphere, with the majority (551
 297 measurements; 73%) in the Pacific (Figure 3), where the water is more corrosive and dis-

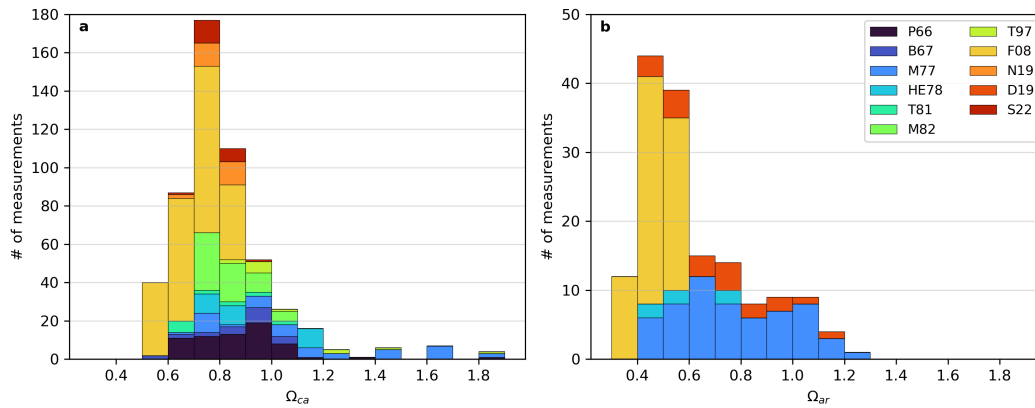


Figure 4. Number of measurements for Ω bins (step-size: 0.1), for (a) calcite and (b) aragonite (note the different scale on y-axis). Measurements with $\Omega > 2$ are omitted (7 measurements). The different studies are colour-coded.

298 solution is expected at shallower depths. The remainder of the measurements (studies
 299 M77 and HE78) were made in the Sargasso Sea in the subtropical North Atlantic. Even
 300 though the experiments do not cover all ocean basins, the experiment sites still capture
 301 a wide range of marine environments (Figure S12).

302 The most frequent way to measure dissolution was determining the weight loss of
 303 a carbonate mineral sample that was placed on a mooring (surface or subsurface moor-
 304 ing) and exposed to seawater for a specific amount of time. A small portion of studies
 305 place their samples in devices that cycled the seawater around the sample to avoid dif-
 306 fusion effects (15% of samples). Apart from weight loss, two other methods have been
 307 used to determine dissolution. One, based on $\delta^{13}\text{C}$, was developed by Subhas et al. (2015)
 308 and is used by the studies that were part of the CDisK-IV cruise (67 measurements; 9%).
 309 The other used surface roughness as a proxy for dissolution (T97; 14 measurements; 1.8%).
 310 A couple of studies additionally record fragmentation of their samples as an indicator
 311 of dissolution (T81 and M82; 79 measurements; 11%). The dissolution rate is reported
 312 either mass-normalised (percentage weight loss per day; 668 measurements; 89%) or mass-
 313 and surface area-normalised (hereafter referred to as surface-normalised; $\text{g cm}^{-2} \text{d}^{-1}$; 163
 314 measurements; 22%), or for HE78 and the CDisK-IV studies, both are provided (80 mea-
 315 surements; 11%).

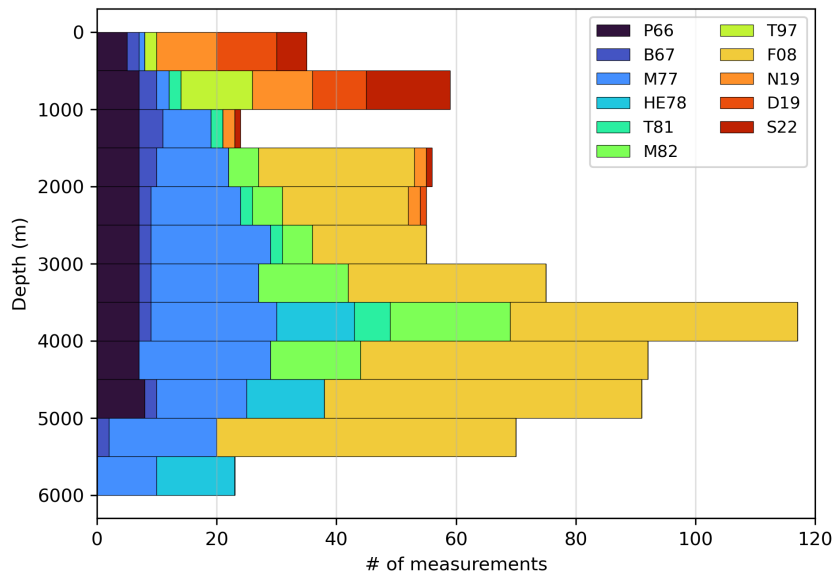


Figure 5. Depth-distribution of the compiled dataset (bin width: 500 m).

316 There is a wide range in the number of measurements each study made: T81 and
 317 T97 contain only 14 measurements each, while F08 contains 298 measurements, mak-
 318 ing up 40% of the dataset (Table 1). A large number of measurements does not neces-
 319 sarily mean a wide range of saturation states: for aragonite in the F08 dataset, Ω is al-
 320 ways below 0.6 (Figure 4b). All F08 data are from deeper than 1000 m (Figure 5), so
 321 shallower CaCO_3 dissolution cannot be investigated with their data. Conversely, the CDisK-
 322 IV studies mostly measured dissolution in the upper 1000 m. The greatest ranges of depth
 323 and saturation states for both calcite and aragonite were achieved by the M77 experi-
 324 ments (162 measurements; 22%).

325 There is a clear trend of higher dissolution rate at lower Ω (Figure 6). Near the sat-
 326 uration horizon ($\Omega = 1$), greater variability in the data and uncertainty in Ω make the
 327 trends more unclear. Since dissolution under these conditions is slower, the rates are closer
 328 to the limit of detection and therefore the signal-to-noise ratio is higher. In general, the
 329 uncertainty in Ω decreases with depth (Figure S13) because at depth there is less vari-
 330 ability in temperature, salinity and oxygen through time.

331 It is notable that dissolution rates at the same saturation state are spread across
 332 2 orders of magnitude even at dissolution further from the saturation horizon. Since al-
 333 most no studies report uncertainties for their dissolution rate measurements (except P66

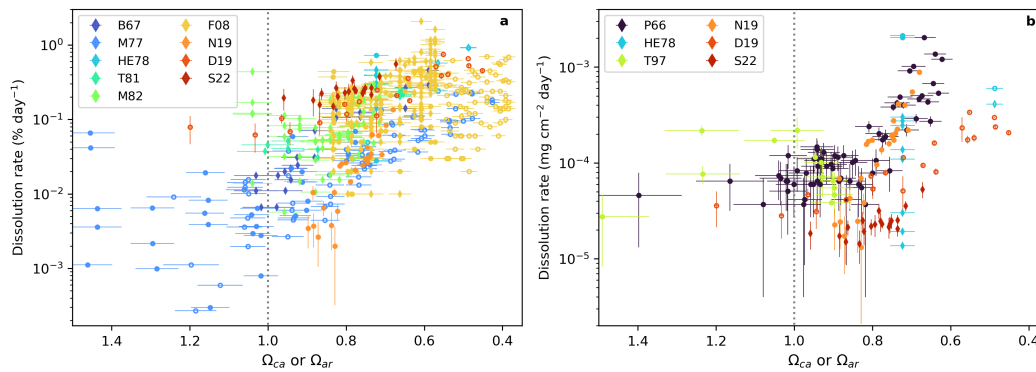


Figure 6. (a) Mass-normalised and (b) surface-normalised dissolution rate as a function of Ω . Open markers denote aragonite, closed markers calcite. Biogenic samples are marked with a diamond and inorganic samples with a circle. Error bars show the 1σ uncertainty in Ω and, if available, the measured dissolution rate (the latter only available for P66, D19, N19 and S22). Data points with $\Omega > 1.5$ are not shown.

334 who gave a constant measurement uncertainty of $\pm 3.3 \times 10^{-5} \text{ g cm}^{-2} \text{ d}^{-1}$ and the CDisK-
 335 IV data with their unique $\delta^{13}\text{C}$ method), it is difficult to say how much of the variation
 336 in the rates can be attributed to measurement uncertainty. However, even studies that
 337 used two of the same kinds of samples at one depth for controls did not see such a spread
 338 in measurements as in Figure 6. Whether this can be attributed to the differences in ex-
 339 perimental design is examined in Section 3.2.

340 Mass-normalised (Figure 6a) and surface-normalised dissolution rates (Figure 6b)
 341 cannot be directly compared with each other if no measurements of the surface area were
 342 reported. The different units can serve different purposes: surface-normalised in situ data
 343 is better suited for comparisons to laboratory measurements since those results are of-
 344 ten expressed this way, while mass-normalised data works better for model comparisons
 345 because models usually only track the mass of particulate inorganic carbon (PIC) in the
 346 water column and not its surface area.

347 Because surface-normalised data try to account for differences in sample size, it is
 348 tempting to assume that they are superior to mass-normalised data. (In general, smaller
 349 samples have a greater surface-to-mass ratio than larger samples, so if samples of dif-
 350 ferent sizes were mass-normalised then we would expect the smaller samples to dissolve
 351 faster.) However, it is questionable which (if any) method of measuring surface area can

352 capture the reactive surface area that is actually available for dissolution (Cubillas et al.,
353 2005). For example, Brunauer-Emmett-Teller (BET) analysis determine the specific sur-
354 face area (SSA) through gas-adsorption, but it has been argued that preparation of bio-
355 genic samples forms micropores which are captured by BET measurements but are un-
356 reactive and unavailable for dissolution (Walter & Morse, 1985; Jeschke & Dreybrodt,
357 2002). Additionally, complex surface shapes can lead to decreased dissolution due to mass-
358 transport limitations (Sulpis et al., 2022; Batchelor-McAuley et al., 2022; Fan et al., 2022).
359 Because the reactive surface area is not captured, surface area measurements can be an
360 additional source of uncertainty. This is demonstrated by HE78: the dissolution of 13
361 different sample types was measured and the rates were expressed as both mass-normalised
362 and surface-normalised. For all samples containing calcite at 5518 m depth, the spread
363 of measured dissolution rates was just over one order of magnitude when normalised to
364 mass but over two orders of magnitude when normalised to mass and surface area.

365 Additionally, if the surface area was not determined with the same method then
366 the data will not be comparable between studies. In the studies presented here, P66 ap-
367 proximates the surface area geometrically, assuming the calcite spheres used were smooth,
368 ignoring potential pits and fractures, Milliman (1977) later notes that the surface area
369 might have been underestimated by a factor of 5. (Milliman (1977) is a correction to nowa-
370 days more widely cited Milliman (1975), with the earlier paper expressing dissolution
371 in surface-normalised terms that the same author later recognises as erroneous.) More
372 recent studies suggest that the difference in crystal surface area (roughness) might re-
373 sult in variability in dissolution rates of up to two orders of magnitude (Wolthers et al.,
374 2012; Lüttge et al., 2013; Agrawal et al., 2021). The P66 rates in Figure 6 can therefore
375 be regarded as an upper bound for the dissolution rate. On the other hand, HE78, N19,
376 D19 and S22 determine the specific surface area (SSA) by BET measurements (HE78
377 with helium gas and N19, D19, and S22 with krypton gas) which results in higher sur-
378 face areas than the geometric approximations and therefore it is expected that on av-
379 erage they obtain lower dissolution rates in their experiments, representing a lower bound
380 for the dissolution rate.

381 Another issue with surface areas becomes apparent in T97: the surface area changes
382 throughout the dissolution process, depending on which dissolution mechanism is preva-
383 lent. In that study, the dissolution rate was determined by measuring surface area rough-
384 ness with Atomic Force Microscopy (AFM). They first assumed a smooth surface and

385 then equated any increase in roughness with dissolution taking place. However, close to
386 equilibrium ($\Omega = 1$), dissolution happens through step edge retreat which can instead
387 smoothen the surface. Dissolution is therefore limited by the number of existing steps
388 on the reactive surface. This mechanism also offers a possible explanation for why the
389 dissolution rate in T97 unexpectedly decreases with Ω : if more dissolution actually de-
390 creases the number of edges instead of forming new etch pits, then surface roughness will
391 not be able to capture the amount of dissolution that actually took place.

392 The change of surface area with ongoing dissolution introduces another problem,
393 especially for studies that last several months. HE78 measured the SSA before and af-
394 ter their experiment and found that the surface area changes were sample-dependent:
395 while for the foraminiferal assemblage the SSA doubled or even tripled, for the coccol-
396 iths it increased by only 10%. The surface-normalised dissolution rate therefore also changes
397 throughout experiments to varying degrees, complicating comparisons between studies
398 or even between samples within a study.

399 To circumvent these issues with surface-normalised dissolution rates, we use only
400 the mass-normalised rates in the following analysis and discussion.

401 **3.2 What drives dissolution and how big is the effect of differing exper-** 402 **imental design?**

403 To investigate the reason for the large spread in the rate measurements for a given
404 saturation state, a machine learning model was trained to predict the mass-normalised
405 dissolution rate from Ω and various features of the experimental design (Section 2.4).

406 The model achieved an R^2 of 0.824 on the test set, so the majority of the variance
407 in dissolution rate was explained. The RMSE and MAE are $0.079 \text{ \% day}^{-1}$ and 0.049
408 \% day^{-1} . The model predicts faster dissolution rates reasonably well but the lower the
409 dissolution rate, the higher the relative error becomes, especially for dissolution rates be-
410 low 0.01 \% day^{-1} (Figure 7). This is due to using squared error as the learning objec-
411 tive for the model, meaning, small absolute errors (which would be large relative errors
412 for low dissolution rates) are ‘punished’ less when the model is trained, leading to worse
413 predictions for the very low rates. However, those rates have higher inherent uncertainty
414 due to being close to the level of detection, so we prioritised good model performance
415 for the higher rates. The worse performance for low dissolution rates could also point

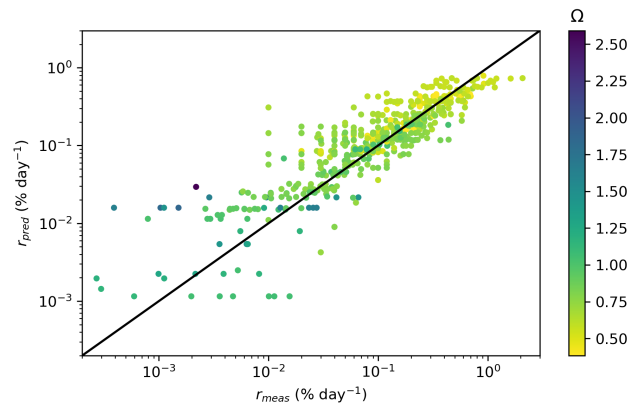


Figure 7. Model predictions of the dissolution rate plotted against the actual measurements.

416 to underfitting, meaning that the model was too simple or lacked the flexibility to cap-
 417 ture the underlying patterns in the data, resulting in higher prediction errors. But due
 418 to the small number of measurements, increasing the model complexity would likely lead
 419 to overfitting, where the model captures noise and random variability in the data at the
 420 expense of the meaningful underlying patterns. We therefore consider the model used
 421 to be the best trade-off between complexity and accuracy.

422 In Figure 8, the model has been used to predict dissolution rates for a range of dif-
 423 ferent saturation states with all possible combinations of the different experimental de-
 424 sign choices that have been made in the in situ studies. The spread in predicted disso-
 425 lution rates for each Ω matches the spread in the actual data. This demonstrates that
 426 the different experimental designs used in the various studies can explain the range of
 427 variation in measured dissolution rates at any given Ω .

428 Permutation Feature Importance gives insight into the relevance of each feature for
 429 the model prediction by measuring the increase in the model's prediction error (here, MSE)
 430 when permutating one feature. Features with permutated (random) values cannot mean-
 431 ingfully contribute to the prediction. In a PFI analysis, this enables us to assess how much
 432 worse the model performs if one feature is not present. Our PFI analysis shows that by
 433 far the most important feature is Ω . All other features in the model have a contribution
 434 that is at most almost an order of magnitude smaller. For the measurement method of
 435 dissolution and the material of the sample, the contributions are completely insignificant
 436 (Figure S14).

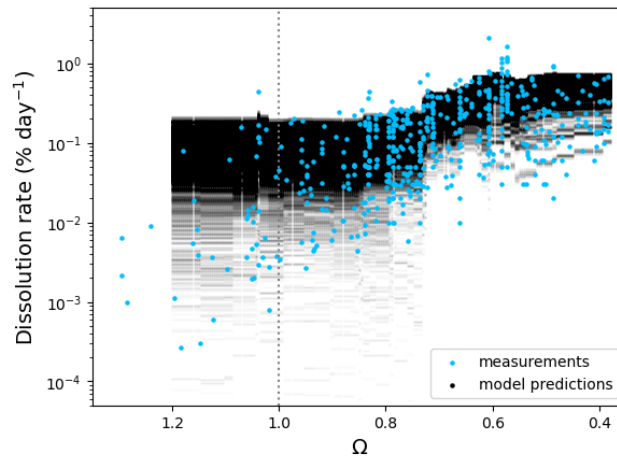


Figure 8. Model predictions for a range of saturation states with all possible combinations of experimental design choices.

437 A drawback of PFI is that the importance of correlated features is shared between
 438 them and some features of the experimental design do covary. For instance, the deploy-
 439 ment time was always very short when dissolution was measured via the $\delta^{13}\text{C}$ method.
 440 The importance of the measurement method might therefore be underestimated and that
 441 of the deployment time overestimated, or vice versa, by our PFI analysis. However, since
 442 the design of the experiment and the water chemistry are mostly independent, our con-
 443 clusion that the measured dissolution rates are mainly determined by Ω should still hold.

444 Partial Dependence Plots show how the predicted dissolution rate varies with each
 445 predictor, revealing the form of the relationship, which could be linear, logarithmic, lo-
 446 gistic, or more complex. If we have some mechanistic understanding of the real-world
 447 system (i.e., we know at least qualitatively what the relationships between predictors and
 448 the model output should be), then PDPs can help to check whether the model makes
 449 sense.

450 Figure 9 shows the PDPs for all features that were used to train the model. For
 451 most of the features, the relationships shown are intuitive and expected: for stronger un-
 452 dersaturation (lower Ω), the model predicts higher dissolution rates (Figure 9a). The jagged-
 453 ness of the line probably results from the datapoints not being evenly distributed along
 454 the Ω range or could be a sign of overfitting, where the PDP is trying to fit the noise in
 455 the data. The bigger the size of the sample, the lower the mass-normalised dissolution

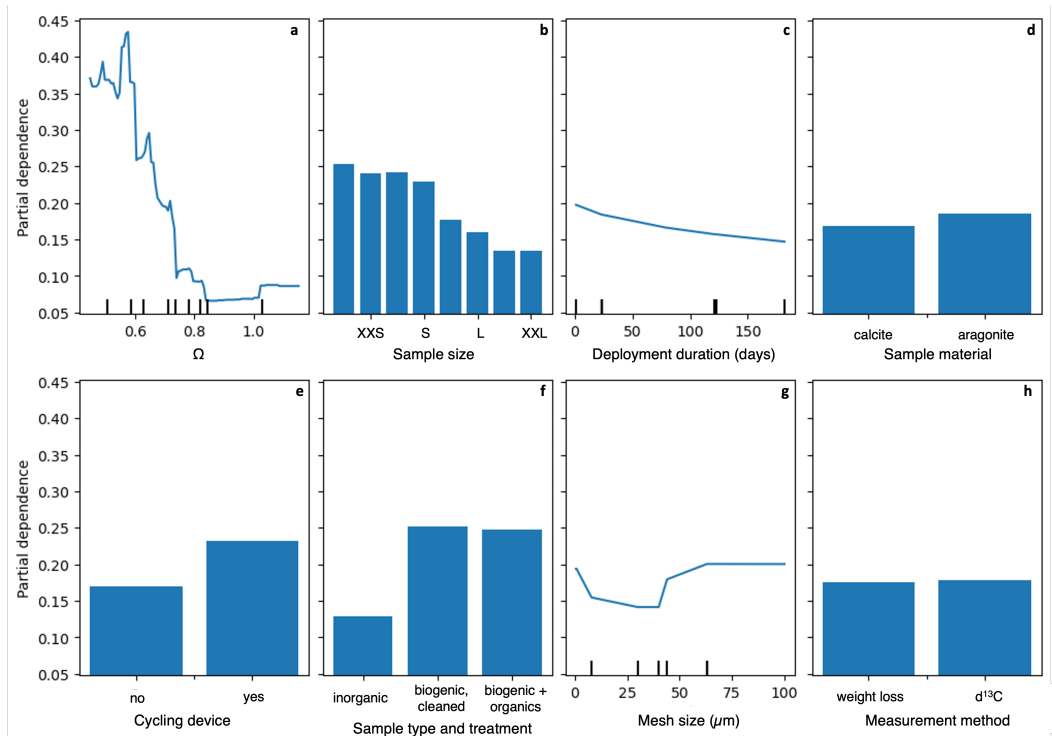


Figure 9. Partial Dependence Plots for all features used in the regression model for the prediction of dissolution rates. Continuous features are represented as a line graph and categorical features as bar graphs. The black lines on the x-axis for continuous features indicate the deciles (10% quantiles). The y-axis is the average predicted dissolution rate.

456 rate, since less surface area is available for dissolution (Figure 9b). Biogenic samples are
 457 predicted to have higher dissolution rates than inorganic samples (Figure 9f), which matches
 458 our understanding that biogenic samples have a higher defect density and therefore should
 459 dissolve faster (e.g., as seen by Busenberg & Niel Plummer, 1989). However, whether
 460 the biogenic samples underwent an oxidative cleaning protocol (bleaching) to remove or-
 461 ganic coatings does not affect the model outcome significantly. This is only directly com-
 462 pared in B67 and HE78 where bleaching the samples increased the dissolution rate. The
 463 presence of a cycling device also leads to higher predictions of dissolution rates (Figure
 464 9e). This could be due to dissolution not being transport-limited (Batchelor-McAuley
 465 et al., 2022; Fan et al., 2022) or because the water flow could break off small pieces of
 466 CaCO_3 which leads to increased weight loss and therefore erroneous rate observations
 467 (as in Metzler et al., 1982).

468 For mesh size, the relationship is more complex. We expected that coarser meshes
469 would lead to higher dissolution rates for two reasons: (i) finer mesh might restrict wa-
470 ter flow around the sample, leading to a pool of water with elevated Ω being trapped around
471 the sample, thus inhibiting dissolution, and (ii) coarser mesh might lead to mechanical
472 loss of the sample which would result in falsely high dissolution rates. However, the model
473 predicts the lowest dissolution rates at intermediate mesh sizes (Figure 9g). One pos-
474 sible reason for this is the lack of training data for mesh sizes above 80 μm . Another is-
475 sue is the assumption of independence of the features in PDPs (Molnar, 2022). When
476 PDPs are calculated, new data points are generated by averaging over marginal distri-
477 butions of other features. These new data points might be unlikely (i.e. very small meshes
478 have only been chosen in combination with water cycling devices when stationary wa-
479 ter is not a problem) or completely unrealistic (i.e. a mesh size that is larger than the
480 size of the sample), which in turn distorts the apparent dependence of the prediction on
481 this feature.

482 There are several ways in which deployment duration can affect the dissolution rate.
483 If the dissolution mechanism leads to increased surface area (as seen in HE78, where SSA
484 was measured both before and after deployment) through etch pit formation, then mass-
485 normalised dissolution should reflect that with increased rates for experiments with longer
486 durations. The opposite seems to be the case here (Figure 9c). One reason could be that
487 the prevalent dissolution mechanism actually decreases the surface area as mentioned
488 in the previous section. Additionally, sample preparation often involved crushing the sam-
489 ples which might have created a greater reactive surface area at the beginning of the de-
490 ployment. Dissolution is then expected to slow down once the initial freshly exposed layer
491 has been dissolved.

492 The gradient of the PDP curves can also indicate feature importance. The results
493 in Figure 9 show similar patterns as the PFI results in Figure S14: the partial depen-
494 dence of predicted dissolution rate changes rapidly with respect to Ω (Figure 9a), indi-
495 cating its relatively high importance as a predictor, whereas for the material of the sam-
496 ple (Figure 9d) and the measurement method (Figure 9h) there is almost no difference
497 in the partial dependence for the different possible predictions, suggesting lower impor-
498 tance.

499 In summary, this machine learning approach is a useful tool that helps us analyse
 500 quantitatively how different features can influence a measured variable by training a model
 501 to predict said variable based on those features. Even though complex tree-based mod-
 502 els often cannot be interpreted directly, several methods exist to help us make sense of
 503 them. Here, the model was able to capture much of the underlying patterns of the data,
 504 which for the most part matched our real-world qualitative understanding of how design
 505 choices should affect the dissolution rate and additionally showed which features affect
 506 it at the most. In practice, this means that only studies designed similarly can be com-
 507 pared directly, with the most important design choices for inter-compatibility being the
 508 particle sizes, inorganic versus biogenic samples, and the presence or absence of a device
 509 that cycles the water around the samples.

510 **3.3 What can in situ measurements tell us despite differences in the ex-** 511 **perimental design?**

512 While our analysis indicated that the majority of the variance in the dissolution
 513 rate was driven by Ω , the differences in experimental design were still significant. There-
 514 fore, while absolute rates might be less meaningful, the patterns of variation with depth,
 515 Ω , and other environmental variables can still give useful insights.

516 As examples, we explore two phenomena in more detail: (i) dissolution above the
 517 saturation horizon and (ii) existence and variability of a critical saturation state Ω_{crit} .

518 ***3.3.1 Dissolution above the saturation horizon***

519 While laboratory experiments measure dissolution only when the bulk water is un-
 520 dersaturated, alkalinity measurements in the ocean indicate that a substantial amount
 521 of carbonate mineral dissolution happens close to the surface where the seawater is over-
 522 saturated. With our new Ω estimates we can now examine whether in situ studies have
 523 also measured dissolution in such conditions.

524 Most studies do not include a significant number of measurements far above the
 525 saturation horizon. Most experiments have been conducted in the Pacific, where Ω val-
 526 ues are on average lower than in other ocean basins and experiments have generally been
 527 focused on depths where water was known or assumed to be close to equilibrium or un-
 528 dersaturated. The only exception is M77 (Figure 4). Below the saturation horizon, dis-

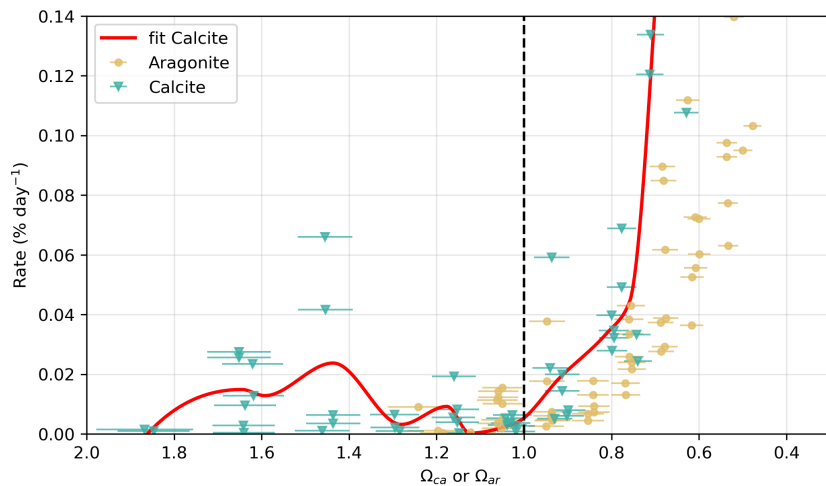


Figure 10. Dissolution rate measurements at the four stations of the M77 experiments for the calcite and aragonite samples as a function of Ω . The error bars represent the uncertainty in Ω . The fit was produced by binning the calcite dissolution rates in Ω -bins of 0.05 and interpolating over the bin-averaged rates.

529 solution follows the expected pattern of increasing non-linearly with lower saturation states
 530 (Figure 10). However, at 3 out of 4 stations where dissolution experiments were conducted,
 531 M77 also observed significant dissolution of their samples at $1.7 > \Omega_{ca} > 1.4$. This
 532 local maximum occurs at 2000 - 2500 m depth (Figure S16), which is far above the lo-
 533 cal saturation horizon for calcite, at approximately 4300 m. This pattern of dissolution
 534 with depth does not match the patterns that are found when estimating dissolution from
 535 alkalinity budgets (Feely et al., 2002; Sulpis et al., 2021) - there, dissolution is highest
 536 closest to the surface, reaching a minimum at around 1000 m, before gradually increas-
 537 ing again. So, what else could this local dissolution maximum?

538 Usually, three possible explanations are given for dissolution in apparently over-
 539 saturated waters: (i) the presence of a more soluble form of carbonate mineral, such as
 540 Mg calcite (Feely et al., 2002; Wilson et al., 2009; Woosley et al., 2012), (ii) dissolution
 541 in the more acidic environment of zooplankton guts (Pond et al., 1995; Milliman et al.,
 542 1999; Jansen & Wolf-Gladrow, 2001), and (iii) other micro-environments, such as ma-
 543 rine snow aggregates, where bacterial oxidation of organic matter can enhance the dis-
 544 solution process (Alldredge & Cohen, 1987; Jansen & Wolf-Gladrow, 2001; Subhas et al.,
 545 2022).

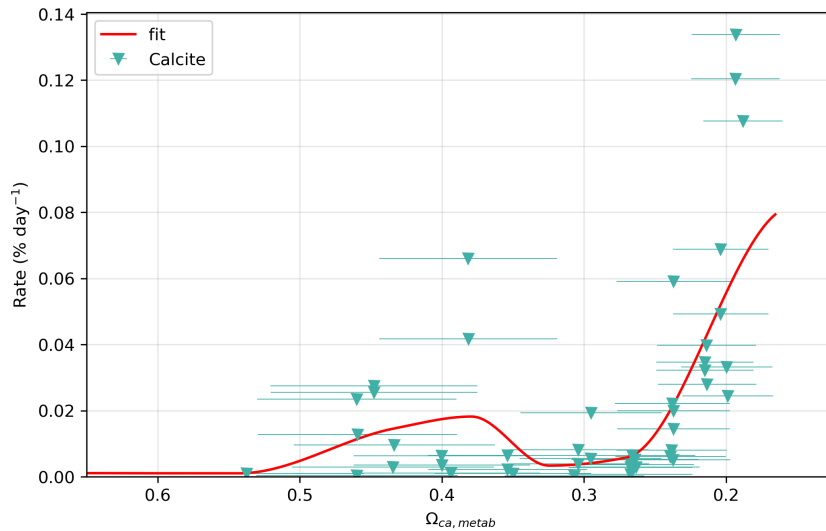


Figure 11. Dissolution rate measurements at the four stations of the M77 experiments for the calcite samples as a function of Ω_{metab} , which was calculated following Subhas et al. (2022). The error bars show the same uncertainty as the original Ω values. The fit was produced by binning the calcite dissolution rates in Ω_{metab} -bins of 0.05 and interpolating over the bin-averaged rates.

546 Hypothesis (i) does not apply in this case because we know that the calcite sam-
 547 ples primarily consisted of *Orbulina universa* and *Globigerinoides sacculifer* which con-
 548 tain little magnesium (< 2%) (Nürnberg et al., 1996). Hypothesis (ii) is equally unlikely:
 549 zooplankton live mainly in the epipelagic and mesopelagic layer (< 1000 m) (Fernández de
 550 Puellas et al., 2019), and the samples were in bags of fine mesh (< 40 μm), so they could
 551 not have been consumed by other organisms.

552 Organic coatings were left intact in M77 and several hundred foraminifera made
 553 up one sample, which could be similar to the marine snow aggregate in hypothesis (iii).
 554 This leaves open the possibility that organic matter degradation could have led to a more
 555 acidic micro-environment. To evaluate the influence of (iii), we calculated Ω_{metab} which
 556 was proposed by Subhas et al. (2022) to account for the degradation and consumption
 557 of organic matter in aggregates where organic carbon and CaCO_3 are closely packed to-
 558 gether. Ω_{metab} is calculated from revised ambient DIC and TA values, which are deter-
 559 mined assuming that all dissolved oxygen in the bulk seawater is metabolised (upper limit
 560 for aerobic metabolic activity). The resulting Ω_{metab} is therefore the lower limit for the
 561 saturation state inside the sample. While the metabolic saturation horizon of calcite is

indeed shallower than the minimum sample depth, so the dissolution no longer appears to have occurred in undersaturated waters, the pattern with Ω_{metab} does not follow Equation 6 (i.e., monotonically increasing) but still has a local maximum (Figure 11) that requires a different explanation. To explain this peak, more is needed. One possibility is the presence of a catalyst that increased the rate of dissolution, such as carbonic anhydrase, as observed by Subhas et al. (2017). Another possibility is that the continued respiration and dissolution proceeded together in a ratio such that the waters stay undersaturated. However, these hypotheses cannot be further examined due to the lack of relevant data. Ultimately, an undersaturated micro-environment due to metabolic activity could explain why dissolution is possible at this depth, but on its own it is insufficient to explain the localised peak at 2000 - 2500 m.

There are more possibilities beyond the three usual explanations discussed above. For instance, (iv) dissolved organic carbon (DOC) binding calcium (Ca) through a chelate effect and thereby lowering the saturation state. Ca has a high affinity to form complexes with organic matter (Raspor et al., 1980), leading to a lower amount of Ca_{free} than what has been calculated from salinity. However, while the DOC concentration is $\sim 50 \mu\text{mol kg}^{-1}$ (Hansell et al., 2021), the Ca concentration is several orders of magnitude larger at $\sim 10 \text{ mmol kg}^{-1}$. The effect of Ca dilution would therefore be negligible. Another hypothesis is that (v) the Ca:CO₃ ratio can affect dissolution, which could also be influenced by complexation of Ca. Stack and Grantham (2010) observed features of dissolution on calcite crystals in oversaturated water at a Ca:CO₃ ratio of 22:1 (highest ratio tested). At the locations and depths of the M77 stations, Ca:CO₃ ratio increases with depth from 110:1 to 190:1. If high Ca:CO₃ ratios allowed dissolution in oversaturated water, then this effect would be true for all samples in the experiment, not just at certain depths, making (v) highly unlikely.

Finding the main driver of this local peak in dissolution would allow us to understand whether it was a consequence of the experiment design, whether it is geographically constrained, and whether it also applies to sinking or suspended particles in the water column. If no explanation is found that describes how dissolution was thermodynamically possible, then (vi) measurement errors would need to be invoked. However, since the duplicates at each depth and at stations separated both temporally (by several months) and spatially (by hundreds of kilometers) showed the same pattern, this seems unlikely. Ultimately, we are unable to explain the dissolution pattern with Ω in

595 M77 with the data available, but if similar features are seen in future studies, measure-
 596 ment of a broader set of auxiliary variables could provide a resolution.

597 **3.3.2 Dissolution regimes**

598 Many in situ studies observe that dissolution starts to rapidly increase at a certain
 599 depth (seen most clearly in P66) at a critical amount of undersaturation. The surface-
 600 normalised data in our compilation also show a faster increase in dissolution rate with
 601 declining Ω at saturation states lower than $\Omega = 0.8$ (Figure 6b). The same is not im-
 602 mediately obvious for the mass-normalised data (Figure 6a) due to the greater scatter
 603 in measured rates. However, the PDP for Ω (based on the model trained on mass-normalised
 604 data only) supports the existence of a change in dissolution rate at a certain Ω value.
 605 When Ω is close to equilibrium, the dissolution rate is barely affected by Ω , but for $\Omega \lesssim$
 606 0.75 the curve becomes much steeper, demonstrating a stronger influence of Ω on the mea-
 607 sured dissolution rate (Figure 9a).

608 Based on the laboratory measurements of Naviaux, Subhas, Rollins, et al. (2019),
 609 N19 and S22 divided their rate measurements into two dissolution regimes, with the bound-
 610 ary at $\Omega_{\text{crit}} = 0.80$ and $\Omega_{\text{crit}} = 0.78$ respectively. However, it is unclear whether these
 611 Ω_{crit} values also produce the best fit for dissolution in the water column where other prop-
 612 erties (e.g., pressure and dissolution inhibitors) could affect Ω_{crit} . Here, we fit the dis-
 613 solution rates in the compilation to two dissolution regimes with a flexible Ω_{crit} (Section
 614 2.5). This works best for studies that have a high Ω resolution over the relevant Ω range
 615 from 0.65 to 0.95.

616 For P66 and M82, the best fit was achieved with Ω_{crit} between 0.80 and 0.87, with
 617 $R^2 > 0.7$ (Figure 12). For comparison, assuming only one dissolution regime with no
 618 Ω_{crit} gave $R^2 < 0.5$ for the same data, a less good fit. The reaction order for the dis-
 619 solution regime where $\Omega < \Omega_{\text{crit}}$, n_2 , was 3.2 for P66 and for M82 it varied between 1.7
 620 (Sample size XS) and 5.0 (Sample size L). This large difference in n_2 for the size frac-
 621 tions in M82 is mainly explained by the different values of Ω_{crit} : the further from equi-
 622 librium Ω_{crit} , the larger n_2 . Contrary to our expectations, dissolution slightly decreases
 623 with decreasing saturation for the three smallest size fractions. Several other studies showed
 624 similar patterns (Figure S17; M77, T81, F08). This may be due to the uncertainty in
 625 the Ω estimation or to measurement errors (not reported in those studies) but we do not

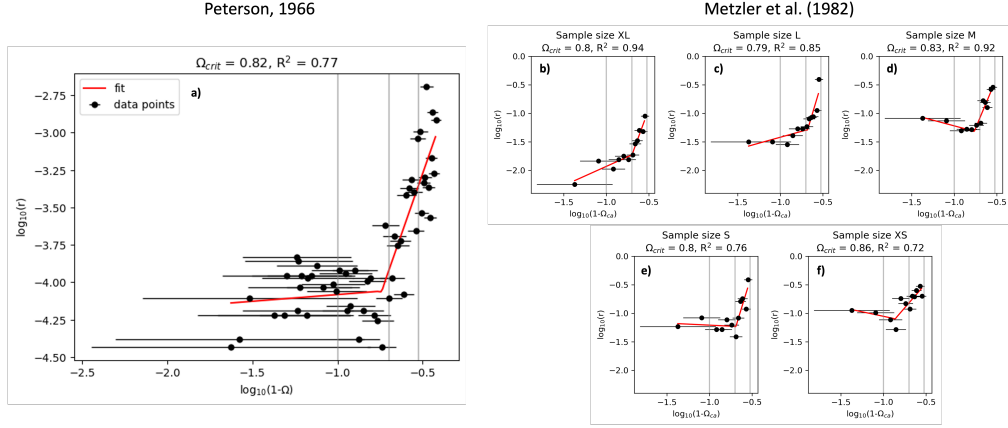


Figure 12. Ω_{crit} for dissolution rates (a) for the calcite pieces in P66 and (b)-(f) foraminifera in different size fractions in M82, determined by fitting to Equation 8. The grey vertical lines mark the saturation state at $\Omega = 0.9, 0.8$ and 0.7 from left to right. The Ω_{crit} value producing the best fit and its corresponding R^2 value are given above each panel.

626 have the necessary information to investigate this further. Examining more studies, it
 627 shows that for this kind of analysis a wide range of Ω with a high resolution of measure-
 628 ments is needed for the most plausible results. The results vary widely if the study has
 629 either few samples or covers a small Ω range: the best fitting Ω_{crit} value is sometimes
 630 as low as 0.6 or as high as 0.95, whereas sometimes none is found at all and n_2 varies
 631 from 0.9 to 15 (Figure S17).

632 Combining all studies with biogenic CaCO_3 samples (the difference in solubility
 633 for calcite and aragonite is already accounted for in the mineral-specific Ω value and as-
 634 suming that the dissolution rate is the same for each mineral at the same Ω (supported
 635 by Figure 9d)), the best fit for mass-normalised dissolution rates was achieved at $\Omega_{\text{crit}} =$
 636 0.8 (Figure 13) with

637
$$r_{\text{slow}} = 0.29 \cdot (1 - \Omega)^{0.76} \tag{9}$$

638
$$r_{\text{fast}} = 2.95 \cdot (1 - \Omega)^{2.29} \tag{10}$$

639 $n_2 = 2.29$ is slightly higher than what was found by S22 ($n_2 = 2.1$) and D19 ($n_2 = 1.76$)
 640 but lower than N19 ($n_2 = 4.7$). The effects of the different experimental designs lead to
 641 a large spread in the data, resulting in a worse fit than in Figure 12, where individual
 642 studies were examined separately. Since the dissolution rate is greatly affected by the
 643 origin of the sample (biogenic or inorganic, Figure 9f), only biogenic samples were in-
 644

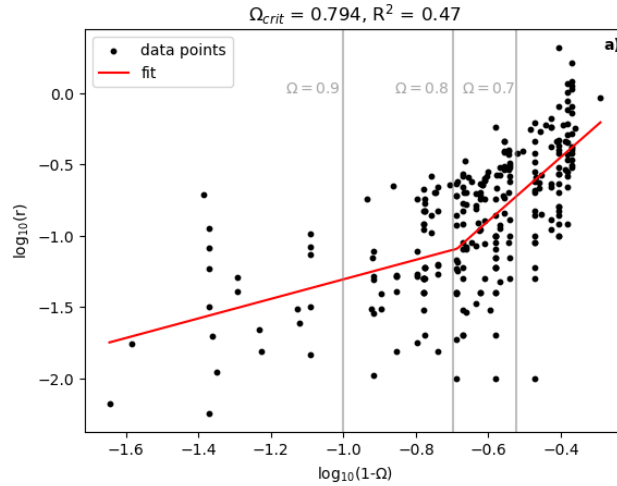


Figure 13. Dissolution rate as a function of Ω_{crit} for all mass-normalised biogenic samples in the compilation. The grey vertical lines mark the saturation state at $\Omega = 0.9, 0.8$ and 0.7 from left to right. The Ω_{crit} value producing the best fit and its corresponding R^2 value are given above the graph.

645 included here. To further reduce the spread of the results, they should be further divided,
 646 for instance by size fraction or whether water cycling devices were employed. However,
 647 in the current dataset this would reduce the number of samples such that no good fits
 648 would be possible because too small an Ω range would be covered.

649 The Ω_{crit} chosen when fitting measurements to equation 6 significantly affects n_2
 650 (reaction order of the fast dissolution regime): with $\Omega_{\text{crit}} = 0.75$, $n_2 = 2.8$ but with
 651 $\Omega_{\text{crit}} = 0.85$, n_2 is just 1.9. For calcite, the effect is minimal in the ocean, since Ω rarely
 652 reaches below 0.6 and at $\Omega = 0.6$, the dissolution rate with $\Omega_{\text{crit}} = 0.75$ is only 10%
 653 faster than with $\Omega_{\text{crit}} = 0.85$. Furthermore, the dissolution rate for calcite at $\Omega = 0.6$
 654 is only increased by 35% when using two dissolution regimes with an intermediate $\Omega_{\text{crit}} =$
 655 0.80 instead of only one with no Ω_{crit} (Figure 14). However, for aragonite, Ω can be around
 656 0.4 at depth. Pteropod shells can sink several hundred meters per day (Noji et al., 1997),
 657 hence they can reach depths with such low saturation states, possibly with further im-
 658 plications such as reducing calcite dissolution by dissolving deeper than expected thus
 659 raising Ω (Sulpis et al., 2022). At $\Omega = 0.4$, the shifting of Ω_{crit} closer or further away
 660 from equilibrium when fitting the data also has more substantial effects: the dissolution
 661 rate with $\Omega_{\text{crit}} = 0.75$ is 25% faster than with $\Omega_{\text{crit}} = 0.80$ and 55% faster than with

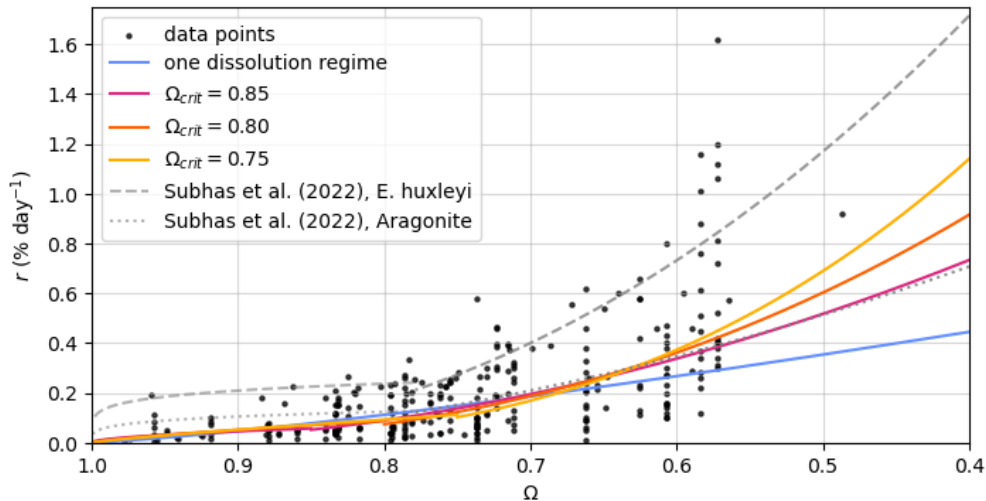


Figure 14. Dissolution rate as a function of Ω , where the rate measurements of biogenic samples were fitted to different Ω_{crit} values or no Ω_{crit} (no change in dissolution mechanism) at all. The fits published in Subhas et al. (2022) for the S22 and D19 data are plotted in grey for comparison.

662 $\Omega_{\text{crit}} = 0.85$. Most notably, the dissolution rate for aragonite at $\Omega = 0.4$ more than
 663 doubles (+106%) when using two dissolution regimes with an intermediate $\Omega_{\text{crit}} = 0.80$
 664 instead of only one with no Ω_{crit} (Figure 14).

665 Overall, the in situ studies suggest that Ω_{crit} is slightly closer to equilibrium in the
 666 water column than the results of the lab experiments by Naviaux, Subhas, Rollins, et
 667 al. (2019) ($\Omega_{\text{crit}} = 0.80$ instead of $\Omega_{\text{crit}} = 0.75$). As a consequence, our compilation
 668 of in situ data suggest that dissolution rates at depth may be slightly lower for calcite
 669 (up to $\sim 3\%$) and significantly lower for aragonite (up to $\sim 20\%$) in the real ocean than
 670 would be expected from laboratory experiments.

671 4 Conclusion

672 In situ experiments account for more real-world complexities than laboratory ex-
 673 periments can. However, published data have not been fully utilised because of missing
 674 hydrographic variables which would make experiments conducted at different study lo-
 675 cations and/or decades apart comparable. Our approach of combining WOA data to-
 676 gether with CANYON-B to estimate a set of carbonate system and other ancillary vari-
 677 ables helps to overcome this issue, adding value to the published data by allowing us to

678 more directly compare them with each other. Our approach could also be applied to other
679 types of experiments and published datasets that do not include a complete set of an-
680 cillary hydrographic variables.

681 In the case of carbonate mineral dissolution we were able to show a wide spread
682 of dissolution rates at the same Ω . While this is partly explained by the choice of sam-
683 ple material, other decisions regarding the experimental design, such as a water cycling
684 device (that removes diffusive transport limitations) and the duration of the deployment,
685 also play a non-negligible role. As a result, the absolute values of measured dissolution
686 rates still cannot be directly compared, but the more qualitative patterns of dissolution
687 rate and its relationship with Ω in the water column still can be. Our analysis confirms
688 that dissolution starts to increase more rapidly at $\Omega_{\text{crit}} \approx 0.8$, confirming that the re-
689 sults of laboratory experiments are applicable in the ocean. To better constrain Ω_{crit} ,
690 future in situ studies should consider measuring dissolution rates with a higher resolu-
691 tion over a wider range of saturation states, as well as performing crystallographic in-
692 vestigations (e.g., AFM) to assess which mechanisms contributed primarily to dissolu-
693 tion at different Ω values.

694 We also found that the only experiment that was conducted in significantly over-
695 saturated water did observe dissolution above the saturation horizon, although no sat-
696 isfactory explanation for this could be found. Due to the lack of ancillary variables, the
697 large scatter in the existing data and the uncertainty of the estimated variables, it was
698 not possible to investigate inhibitors to dissolution or other drivers of dissolution, apart
699 from Ω . Conducting more in situ experiments in a range of different marine environments
700 (e.g., Pacific and Atlantic) but with the same experimental design and sample types could
701 help to disentangle the effects of other variables and close the major gaps in our funda-
702 mental understanding of marine carbonate mineral dissolution.

703 **Open Research**

704 The compiled data set with all the added ancillary information can be found in [https://](https://doi.org/10.25850/nioz/7b.b.bg)
705 doi.org/10.25850/nioz/7b.b.bg. The Python and MATLAB scripts to compile the
706 data and estimate Ω as well as the python script to generate all the figures in the main
707 text and the SI is available at <https://github.com/bcala1/in-situ-dissolution-compilation>.

708 **Acknowledgments**

709 The authors would like thank all the scientists and crews who over the last six decades
 710 collected and published the in situ dissolution rates on which this analysis is based on.
 711 This research was funded by the UU-NIOZ collaboration project, “BEYOND the known
 712 drivers of marine carbonate mineral dissolution: closing the gap in the alkalinity bud-
 713 get” (project number NZ4543.25). This project has received funding from the European
 714 Research Council (ERC) under the European Union’s Horizon 2020 research and inno-
 715 vation programme (grant agreement No. [819588]). OS was supported by the Nether-
 716 lands Organisation for Scientific Research (NWO-VENI Grant VI.Veni.212.086).

717 **References**

- 718 Agrawal, P., Bollermann, T., Raoof, A., Iliev, O., Fischer, C., & Wolthers, M. (2021,
 719 August). The contribution of hydrodynamic processes to calcite dissolution
 720 rates and rate spectra. *Geochimica et Cosmochimica Acta*, *307*, 338–350.
 721 Retrieved 2023-07-05, from [https://www.sciencedirect.com/science/](https://www.sciencedirect.com/science/article/pii/S0016703721002660)
 722 [article/pii/S0016703721002660](https://www.sciencedirect.com/science/article/pii/S0016703721002660) doi: 10.1016/j.gca.2021.05.003
- 723 Alldredge, A. L., & Cohen, Y. (1987, February). Can Microscale Chemical Patches
 724 Persist in the Sea? Microelectrode Study of Marine Snow, Fecal Pellets. *Sci-*
 725 *ence*, *235*(4789), 689–691. Retrieved 2023-07-23, from [https://www.science](https://www.science.org/doi/10.1126/science.235.4789.689)
 726 [.org/doi/10.1126/science.235.4789.689](https://www.science.org/doi/10.1126/science.235.4789.689) (Publisher: American Associa-
 727 tion for the Advancement of Science) doi: 10.1126/science.235.4789.689
- 728 Archer, D., Eby, M., Brovkin, V., Ridgwell, A., Cao, L., Mikolajewicz, U., ...
 729 Tokos, K. (2009, May). Atmospheric Lifetime of Fossil Fuel Carbon Diox-
 730 ide. *Annual Review of Earth and Planetary Sciences*, *37*(1), 117–134. Re-
 731 trieved 2023-07-12, from [https://www.annualreviews.org/doi/10.1146/](https://www.annualreviews.org/doi/10.1146/annurev.earth.031208.100206)
 732 [annurev.earth.031208.100206](https://www.annualreviews.org/doi/10.1146/annurev.earth.031208.100206) doi: 10.1146/annurev.earth.031208.100206
- 733 Batchelor-McAuley, C., Yang, M., Rickaby, R. E. M., & Compton, R. G.
 734 (2022). Calcium Carbonate Dissolution from the Laboratory to the
 735 Ocean: Kinetics and Mechanism. *Chemistry – A European Jour-*
 736 *nal*, *28*(68), e202202290. Retrieved 2023-07-14, from [https://](https://onlinelibrary.wiley.com/doi/abs/10.1002/chem.202202290)
 737 onlinelibrary.wiley.com/doi/abs/10.1002/chem.202202290 (eprint:
 738 <https://onlinelibrary.wiley.com/doi/pdf/10.1002/chem.202202290>) doi:
 739 10.1002/chem.202202290

- 740 Berelson, W. M., Adkins, J. F., Subhas, A. V., Dong, S., & Naviaux, J. D. (2022,
741 August). *In situ experimentally determined dissolution rates of biogenic cal-*
742 *cites along a North Pacific transect between Hawaii and Alaska (KM1712*
743 *expedition) in August 2017.* Biological and Chemical Oceanography Data
744 Management Office (BCO-DMO). Retrieved 2023-07-04, from [https://](https://hdl.handle.net/1912/29186)
745 hdl.handle.net/1912/29186 doi: 10.26008/1912/BCO-DMO.856409.2
- 746 Berger, W. H. (1967, April). Foraminiferal Ooze: Solution at Depths. *Science*,
747 *156*(3773), 383–385. Retrieved 2022-03-27, from [https://www.science.org/](https://www.science.org/doi/abs/10.1126/science.156.3773.383)
748 [doi/abs/10.1126/science.156.3773.383](https://www.science.org/doi/abs/10.1126/science.156.3773.383) (Publisher: American Association
749 for the Advancement of Science) doi: 10.1126/science.156.3773.383
- 750 Bittig, H. C., Steinhoff, T., Claustre, H., Fiedler, B., Williams, N. L., Sauzède, R.,
751 ... Gattuso, J.-P. (2018). An Alternative to Static Climatologies: Robust Es-
752 timation of Open Ocean CO₂ Variables and Nutrient Concentrations From T,
753 S, and O₂ Data Using Bayesian Neural Networks. *Frontiers in Marine Science*,
754 *5*. Retrieved 2022-03-03, from [https://www.frontiersin.org/article/](https://www.frontiersin.org/article/10.3389/fmars.2018.00328)
755 [10.3389/fmars.2018.00328](https://www.frontiersin.org/article/10.3389/fmars.2018.00328)
- 756 Breiman, L. (2001a). Random Forests. *Machine Learning*, *45*(1), 5–32. Retrieved
757 2023-03-28, from <http://link.springer.com/10.1023/A:1010933404324>
758 doi: 10.1023/A:1010933404324
- 759 Breiman, L. (2001b). Statistical modeling: The two cultures (with comments and a
760 rejoinder by the author). *Statistical science*, *16*(3), 199–231. (Publisher: Insti-
761 tute of Mathematical Statistics)
- 762 Breiman, L., Friedman, J., Stone, C. J., & Olshen, R. A. (1984). *Classification and*
763 *regression trees.* CRC press.
- 764 Buitenhuis, E. T., Le Quéré, C., Bednaršek, N., & Schiebel, R. (2019). Large
765 Contribution of Pteropods to Shallow CaCO₃ Export. *Global Biogeo-*
766 *chemical Cycles*, *33*(3), 458–468. Retrieved 2023-07-06, from [https://](https://onlinelibrary.wiley.com/doi/abs/10.1029/2018GB006110)
767 onlinelibrary.wiley.com/doi/abs/10.1029/2018GB006110 (eprint:
768 <https://onlinelibrary.wiley.com/doi/pdf/10.1029/2018GB006110>) doi:
769 [10.1029/2018GB006110](https://onlinelibrary.wiley.com/doi/pdf/10.1029/2018GB006110)
- 770 Busenberg, E., & Niel Plummer, L. (1989, June). Thermodynamics of magne-
771 sian calcite solid-solutions at 25°C and 1 atm total pressure. *Geochim-*
772 *ica et Cosmochimica Acta*, *53*(6), 1189–1208. Retrieved 2023-10-01, from

- 773 <https://www.sciencedirect.com/science/article/pii/0016703789900562>
774 doi: 10.1016/0016-7037(89)90056-2
- 775 Chen, T., & Guestrin, C. (2016, August). XGBoost: A Scalable Tree Boosting Sys-
776 tem. In *Proceedings of the 22nd ACM SIGKDD International Conference on*
777 *Knowledge Discovery and Data Mining* (pp. 785–794). New York, NY, USA:
778 Association for Computing Machinery. Retrieved 2022-08-21, from [https://](https://doi.org/10.1145/2939672.2939785)
779 doi.org/10.1145/2939672.2939785 doi: 10.1145/2939672.2939785
- 780 Cubillas, P., Köhler, S., Prieto, M., Chairat, C., & Oelkers, E. H. (2005, March). Ex-
781 perimental determination of the dissolution rates of calcite, aragonite, and bi-
782 valves. *Chemical Geology*, *216*(1), 59–77. Retrieved 2022-07-05, from [https://](https://www.sciencedirect.com/science/article/pii/S0009254104004589)
783 www.sciencedirect.com/science/article/pii/S0009254104004589 doi:
784 10.1016/j.chemgeo.2004.11.009
- 785 Dickson, A. G. (1990, February). Standard potential of the reaction: $\text{AgCl(s)} +$
786 $12\text{H}_2\text{(g)} = \text{Ag(s)} + \text{HCl(aq)}$, and the standard acidity constant of the
787 ion HSO_4^- in synthetic sea water from 273.15 to 318.15 K. *The Journal of*
788 *Chemical Thermodynamics*, *22*(2), 113–127. Retrieved 2023-07-06, from
789 <https://www.sciencedirect.com/science/article/pii/002196149090074Z>
790 doi: 10.1016/0021-9614(90)90074-Z
- 791 Dong, S., Berelson, W. M., Rollins, N. E., Subhas, A. V., Naviaux, J. D., Celes-
792 tian, A. J., ... Adkins, J. F. (2019, June). Aragonite dissolution kinet-
793 ics and calcite/aragonite ratios in sinking and suspended particles in the
794 North Pacific. *Earth and Planetary Science Letters*, *515*, 1–12. Retrieved
795 2022-03-27, from [https://www.sciencedirect.com/science/article/pii/](https://www.sciencedirect.com/science/article/pii/S0012821X19301645)
796 [S0012821X19301645](https://www.sciencedirect.com/science/article/pii/S0012821X19301645) doi: 10.1016/j.epsl.2019.03.016
- 797 Dong, S., Liu, X., Naviaux, J. D., Subhas, A. V., Rollins, N. E., Adkins, J. F., &
798 Berelson, W. M. (2022, February). *Carbonate chemistry and CTD data col-*
799 *lected along a North Pacific transect between Hawaii and Alaska on R/V Kilo*
800 *Moana cruise KM1712 in August 2017*. Biological and Chemical Oceanography
801 Data Management Office (BCO-DMO). Retrieved 2023-10-11, from [https://](https://hdl.handle.net/1912/27970)
802 hdl.handle.net/1912/27970 doi: 10.26008/1912/BCO-DMO.836954.2
- 803 Edmond, J. M. (1974, June). On the dissolution of carbonate and silicate in the
804 deep ocean. *Deep Sea Research and Oceanographic Abstracts*, *21*(6), 455–
805 480. Retrieved 2023-07-22, from <https://www.sciencedirect.com/science/>

- 806 [article/pii/0011747174900941](#) doi: 10.1016/0011-7471(74)90094-1
- 807 Fan, X., Batchelor-McAuley, C., Yang, M., & Compton, R. G. (2022, October).
808 Single Calcite Particle Dissolution Kinetics: Revealing the Influence of Mass
809 Transport. *ACS Measurement Science Au*, 2(5), 422–429. Retrieved 2023-10-
810 01, from <https://doi.org/10.1021/acsmeasuresciau.2c00025> (Publisher:
811 American Chemical Society) doi: 10.1021/acsmeasuresciau.2c00025
- 812 Feely, R. A., Sabine, C. L., Lee, K., Millero, F. J., Lamb, M. F., Greeley, D., ...
813 Wong, C. S. (2002). In situ calcium carbonate dissolution in the Pacific Ocean.
814 *Global Biogeochemical Cycles*, 16(4), 91–1–91–12. Retrieved 2023-07-17,
815 from <https://onlinelibrary.wiley.com/doi/abs/10.1029/2002GB001866>
816 (eprint: <https://onlinelibrary.wiley.com/doi/pdf/10.1029/2002GB001866>) doi:
817 10.1029/2002GB001866
- 818 Fernández de Puelles, M. L., Gazá, M., Cabanellas-Reboredo, M., Santandreu,
819 M. d. M., Irigoien, X., González-Gordillo, J. I., ... Hernández-León, S.
820 (2019, November). Zooplankton Abundance and Diversity in the Tropical
821 and Subtropical Ocean. *Diversity*, 11(11), 203. Retrieved 2023-09-28, from
822 <https://www.mdpi.com/1424-2818/11/11/203> (Number: 11 Publisher:
823 Multidisciplinary Digital Publishing Institute) doi: 10.3390/d11110203
- 824 Friedman, J. H. (2001). Greedy Function Approximation: A Gradient Boosting
825 Machine. *The Annals of Statistics*, 29(5), 1189–1232. Retrieved 2023-05-
826 16, from <https://www.jstor.org/stable/2699986> (Publisher: Institute of
827 Mathematical Statistics)
- 828 Fukuhara, T., Tanaka, Y., Ioka, N., & Nishimura, A. (2008, January). An in situ
829 experiment of calcium carbonate dissolution in the central Pacific Ocean.
830 *International Journal of Greenhouse Gas Control*, 2(1), 78–88. Retrieved
831 2022-04-22, from [https://www.sciencedirect.com/science/article/pii/](https://www.sciencedirect.com/science/article/pii/S1750583607000850)
832 [S1750583607000850](https://www.sciencedirect.com/science/article/pii/S1750583607000850) doi: 10.1016/S1750-5836(07)00085-0
- 833 Garcia, H., Weathers, K., Paver, C., Smolyar, I., Boyer, T., Locarnini, M., ... Rea-
834 gan, J. (2019, January). *World Ocean Atlas 2018, Volume 3: Dissolved Oxy-*
835 *gen, Apparent Oxygen Utilization, and Dissolved Oxygen Saturation*. Retrieved
836 2023-05-16, from <https://archimer.ifremer.fr/doc/00651/76337/>
- 837 Gehlen, M., Bassinot, F. C., Chou, L., & McCorkle, D. (2005, August). Reassessing
838 the dissolution of marine carbonates: II. Reaction kinetics. *Deep Sea Re-*

- 839 search Part I: *Oceanographic Research Papers*, 52(8), 1461–1476. Retrieved
840 2022-04-26, from [https://www.sciencedirect.com/science/article/pii/](https://www.sciencedirect.com/science/article/pii/S0967063705001068)
841 S0967063705001068 doi: 10.1016/j.dsr.2005.03.011
- 842 Hansell, D. A., Carlson, C. A., Amon, R. M. W., Álvarez Salgado, X. A., Ya-
843 mashita, Y., Romera-Castillo, C., & Bif, M. B. (2021). *Compilation of*
844 *dissolved organic matter (DOM) data obtained from global ocean observa-*
845 *tions from 1994 to 2021. Version 2. (NCEI Accession 0227166).* NOAA
846 National Centers for Environmental Information. Retrieved 2023-10-06,
847 from <https://www.ncei.noaa.gov/archive/accession/0227166> doi:
848 10.25921/S4F4-YE35
- 849 Hawley, J., & Pytkowicz, R. M. (1969, December). Solubility of calcium carbon-
850 ate in seawater at high pressures and 2°C. *Geochimica et Cosmochimica Acta*,
851 33(12), 1557–1561. Retrieved 2023-07-12, from [https://www.sciencedirect](https://www.sciencedirect.com/science/article/pii/0016703769901562)
852 [.com/science/article/pii/0016703769901562](https://www.sciencedirect.com/science/article/pii/0016703769901562) doi: 10.1016/0016-7037(69)
853 90156-2
- 854 Honjo, S., & Erez, J. (1978, July). Dissolution rates of calcium carbonate in
855 the deep ocean; an in-situ experiment in the North Atlantic Ocean. *Earth*
856 *and Planetary Science Letters*, 40(2), 287–300. Retrieved 2022-03-27, from
857 <https://www.sciencedirect.com/science/article/pii/0012821X78900997>
858 doi: 10.1016/0012-821X(78)90099-7
- 859 Humphreys, M. P., Lewis, E. R., Sharp, J. D., & Pierrot, D. (2022, January).
860 PyCO2SYS v1.8: marine carbonate system calculations in Python. *Geo-*
861 *scientific Model Development*, 15(1), 15–43. Retrieved 2023-06-29, from
862 <https://gmd.copernicus.org/articles/15/15/2022/> (Publisher: Coperni-
863 cus GmbH) doi: 10.5194/gmd-15-15-2022
- 864 Jansen, H., & Wolf-Gladrow, D. (2001). Carbonate dissolution in copepod guts:
865 a numerical model. *Marine Ecology Progress Series*, 221, 199–207. Re-
866 trieved 2023-07-06, from [http://www.int-res.com/abstracts/meps/v221/](http://www.int-res.com/abstracts/meps/v221/p199-207/)
867 p199-207/ doi: 10.3354/meps221199
- 868 Jeschke, A. A., & Dreybrodt, W. (2002, September). Dissolution rates of
869 minerals and their relation to surface morphology. *Geochimica et Cos-*
870 *mochimica Acta*, 66(17), 3055–3062. Retrieved 2023-09-27, from [https://](https://www.sciencedirect.com/science/article/pii/S0016703702008931)
871 www.sciencedirect.com/science/article/pii/S0016703702008931 doi:

- 872 10.1016/S0016-7037(02)00893-1
- 873 Keir, R. S. (1980, February). The dissolution kinetics of biogenic calcium carbonates
874 in seawater. *Geochimica et Cosmochimica Acta*, 44(2), 241–252. Retrieved
875 2022-04-26, from [https://www.sciencedirect.com/science/article/pii/](https://www.sciencedirect.com/science/article/pii/S0016703780901350)
876 0016703780901350 doi: 10.1016/0016-7037(80)90135-0
- 877 Lauvset, S. K., Lange, N., Tanhua, T., Bittig, H. C., Olsen, A., Kozyr, A., ...
878 Key, R. M. (2022, December). GLODAPv2.2022: the latest version of
879 the global interior ocean biogeochemical data product. *Earth System Sci-*
880 *ence Data*, 14(12), 5543–5572. Retrieved 2023-06-29, from [https://](https://essd.copernicus.org/articles/14/5543/2022/)
881 essd.copernicus.org/articles/14/5543/2022/ (Publisher: Copernicus
882 GmbH) doi: 10.5194/essd-14-5543-2022
- 883 Liang, H., Lunstrum, A. M., Dong, S., Berelson, W. M., & John, S. G.
884 (2023). Constraining CaCO₃ Export and Dissolution With an
885 Ocean Alkalinity Inverse Model. *Global Biogeochemical Cycles*,
886 37(2), e2022GB007535. Retrieved 2023-05-16, from [https://](https://onlinelibrary.wiley.com/doi/abs/10.1029/2022GB007535)
887 onlinelibrary.wiley.com/doi/abs/10.1029/2022GB007535 (eprint:
888 <https://agupubs.onlinelibrary.wiley.com/doi/pdf/10.1029/2022GB007535>) doi:
889 10.1029/2022GB007535
- 890 Locarnini, M., Mishonov, A., Baranova, O., Boyer, T., Zweng, M., Garcia, H., ...
891 Smolyar, I. (2018, January). *World Ocean Atlas 2018, Volume 1: Tempera-*
892 *ture*. Retrieved 2023-05-16, from [https://archimer.ifremer.fr/doc/00651/](https://archimer.ifremer.fr/doc/00651/76338/)
893 76338/
- 894 Lüttge, A., Arvidson, R. S., & Fischer, C. (2013, June). A Stochastic Treatment
895 of Crystal Dissolution Kinetics. *Elements*, 9(3), 183–188. Retrieved 2023-
896 05-16, from <https://doi.org/10.2113/gselements.9.3.183> doi: 10.2113/
897 gselements.9.3.183
- 898 Metzler, C. V., Wenkam, C. R., & Berger, W. H. (1982, October). Dissolution of
899 foraminifera in the eastern equatorial Pacific; an in situ experiment. *Journal of*
900 *Foraminiferal Research*, 12(4), 362–368. Retrieved 2022-04-25, from [https://](https://doi.org/10.2113/gsjfr.12.4.362)
901 doi.org/10.2113/gsjfr.12.4.362 doi: 10.2113/gsjfr.12.4.362
- 902 Milliman, J. D. (1975, August). Dissolution of aragonite, Mg-calcite, and calcite in
903 the North Atlantic Ocean. *Geology*, 3(8), 461–462. Retrieved 2022-04-22, from
904 [https://doi.org/10.1130/0091-7613\(1975\)3<461:DOAMAC>2.0.CO;2](https://doi.org/10.1130/0091-7613(1975)3<461:DOAMAC>2.0.CO;2) doi:

- 905 10.1130/0091-7613(1975)3(461:DOAMAC)2.0.CO;2
- 906 Milliman, J. D. (1977). Dissolution of calcium carbonate in the Sargasso Sea (north-
907 west Atlantic). *The fate of fossil fuel CO₂ in the oceans*, 641–653. (Publisher:
908 Springer US)
- 909 Milliman, J. D., Troy, P. J., Balch, W. M., Adams, A. K., Li, Y. H., & Mackenzie,
910 F. T. (1999, October). Biologically mediated dissolution of calcium carbon-
911 ate above the chemical lysocline? *Deep Sea Research Part I: Oceanographic
912 Research Papers*, 46(10), 1653–1669. Retrieved 2022-04-22, from [https://
913 www.sciencedirect.com/science/article/pii/S0967063799000345](https://www.sciencedirect.com/science/article/pii/S0967063799000345) doi:
914 10.1016/S0967-0637(99)00034-5
- 915 Molnar, C. (2022). *Interpretable Machine Learning: A Guide for Making
916 Black Box Models Explainable* (2nd ed.). Retrieved 2023-05-16, from
917 <https://christophm.github.io/interpretable-ml-book/>
- 918 Morse, J. W., & Arvidson, R. S. (2002, July). The dissolution kinetics of major sed-
919 imentary carbonate minerals. *Earth-Science Reviews*, 58(1), 51–84. Retrieved
920 2022-04-22, from [https://www.sciencedirect.com/science/article/pii/
921 S0012825201000836](https://www.sciencedirect.com/science/article/pii/S0012825201000836) doi: 10.1016/S0012-8252(01)00083-6
- 922 Morse, J. W., & Berner, R. A. (1972, November). Dissolution kinetics of cal-
923 cium carbonate in sea water; I, A kinetic origin for the lysocline. *Amer-
924 ican Journal of Science*, 272(9), 840–851. Retrieved 2023-07-05, from
925 <https://ajs.scholasticahq.com/article/59569> (Publisher: American
926 Journal of Science) doi: 10.2475/ajs.272.9.840
- 927 Mucci, A. (1983, September). The solubility of calcite and aragonite in seawater at
928 various salinities, temperatures, and one atmosphere total pressure. *American
929 Journal of Science*, 283(7), 780–799. Retrieved 2022-04-26, from [https://www
930 .ajsonline.org/content/283/7/780](https://www.ajsonline.org/content/283/7/780) (Publisher: American Journal of Sci-
931 ence Section: Articles) doi: 10.2475/ajs.283.7.780
- 932 Naviaux, J. D., Subhas, A. V., Dong, S., Rollins, N. E., Liu, X., Byrne, R. H.,
933 ... Adkins, J. F. (2019, September). Calcite dissolution rates in sea-
934 water: Lab vs. in-situ measurements and inhibition by organic matter.
935 *Marine Chemistry*, 215, 103684. Retrieved 2022-04-01, from [https://
936 www.sciencedirect.com/science/article/pii/S0304420319300763](https://www.sciencedirect.com/science/article/pii/S0304420319300763) doi:
937 10.1016/j.marchem.2019.103684

- 938 Naviaux, J. D., Subhas, A. V., Rollins, N. E., Dong, S., Berelson, W. M., & Adkins,
939 J. F. (2019, February). Temperature dependence of calcite dissolution kinet-
940 ics in seawater. *Geochimica et Cosmochimica Acta*, *246*, 363–384. Retrieved
941 2023-07-05, from [https://www.sciencedirect.com/science/article/pii/](https://www.sciencedirect.com/science/article/pii/S0016703718306677)
942 [S0016703718306677](https://www.sciencedirect.com/science/article/pii/S0016703718306677) doi: 10.1016/j.gca.2018.11.037
- 943 Neukermans, G., Bach, L. T., Butterley, A., Sun, Q., Claustre, H., & Fournier,
944 G. R. (2023, April). Quantitative and mechanistic understanding of the
945 open ocean carbonate pump - perspectives for remote sensing and autonomous
946 in situ observation. *Earth-Science Reviews*, *239*, 104359. Retrieved 2023-
947 10-14, from [https://www.sciencedirect.com/science/article/pii/](https://www.sciencedirect.com/science/article/pii/S001282522300048X)
948 [S001282522300048X](https://www.sciencedirect.com/science/article/pii/S001282522300048X) doi: 10.1016/j.earscirev.2023.104359
- 949 Noji, T. T., Bathmann, U. V., Bodungen, B. v., Voss, M., Antia, A., Krumbholz,
950 M., ... Rey, F. (1997, July). Clearance of picoplankton-sized particles and
951 formation of rapidly sinking aggregates by the pteropod, *Limacina reiroversa*.
952 *Journal of Plankton Research*, *19*(7), 863–875. Retrieved 2023-09-27, from
953 <https://doi.org/10.1093/plankt/19.7.863> doi: 10.1093/plankt/19.7.863
- 954 Nürnberg, D., Bijma, J., & Hemleben, C. (1996, March). Assessing the reliability
955 of magnesium in foraminiferal calcite as a proxy for water mass temperatures.
956 *Geochimica et Cosmochimica Acta*, *60*(5), 803–814. Retrieved 2023-07-12, from
957 <https://www.sciencedirect.com/science/article/pii/0016703795004467>
958 doi: 10.1016/0016-7037(95)00446-7
- 959 Olsen, A., Key, R. M., van Heuven, S., Lauvset, S. K., Velo, A., Lin, X., ... Suzuki,
960 T. (2016, August). The Global Ocean Data Analysis Project version 2
961 (GLODAPv2) – an internally consistent data product for the world ocean.
962 *Earth System Science Data*, *8*(2), 297–323. Retrieved 2023-06-29, from
963 <https://essd.copernicus.org/articles/8/297/2016/> (Publisher: Coper-
964 nicus GmbH) doi: 10.5194/essd-8-297-2016
- 965 Orr, J. C., Epitalon, J.-M., Dickson, A. G., & Gattuso, J.-P. (2018, Novem-
966 ber). Routine uncertainty propagation for the marine carbon dioxide sys-
967 tem. *Marine Chemistry*, *207*, 84–107. Retrieved 2023-07-02, from [https://](https://www.sciencedirect.com/science/article/pii/S030442031830149X)
968 www.sciencedirect.com/science/article/pii/S030442031830149X doi:
969 10.1016/j.marchem.2018.10.006
- 970 Patsavas, M. C., Byrne, R. H., Wanninkhof, R., Feely, R. A., & Cai, W.-J. (2015,

- 971 November). Internal consistency of marine carbonate system measurements
972 and assessments of aragonite saturation state: Insights from two U.S. coastal
973 cruises. *Marine Chemistry*, 176, 9–20. Retrieved 2023-07-11, from [https://](https://www.sciencedirect.com/science/article/pii/S0304420315300074)
974 www.sciencedirect.com/science/article/pii/S0304420315300074 doi:
975 10.1016/j.marchem.2015.06.022
- 976 Pedregosa, F., Varoquaux, G., Gramfort, A., Michel, V., Thirion, B., Grisel, O., ...
977 Duchesnay, E. (2011). Scikit-learn: Machine Learning in Python. *Journal of*
978 *Machine Learning Research*, 12(85), 2825–2830. Retrieved 2023-05-16, from
979 <http://jmlr.org/papers/v12/pedregosa11a.html>
- 980 Peterson, M. N. A. (1966, December). Calcite: Rates of Dissolution in a
981 Vertical Profile in the Central Pacific. *Science*, 154(3756), 1542–1544.
982 Retrieved 2022-03-21, from [https://www.science.org/doi/10.1126/](https://www.science.org/doi/10.1126/science.154.3756.1542)
983 [science.154.3756.1542](https://www.science.org/doi/10.1126/science.154.3756.1542) (Publisher: American Association for the Ad-
984 vancement of Science) doi: 10.1126/science.154.3756.1542
- 985 Pond, D. W., Harris, R. P., & Brownlee, C. (1995, July). A microinjection tech-
986 nique using a pH-sensitive dye to determine the gut pH of *Calanus hel-*
987 *golandicus*. *Marine Biology*, 123(1), 75–79. Retrieved 2023-07-06, from
988 <https://doi.org/10.1007/BF00350325> doi: 10.1007/BF00350325
- 989 Raspor, B., Nürnberg, H. W., Valenta, P., & Branica, M. (1980, December). Kinetics
990 and mechanism of trace metal chelation in sea water. *Journal of Electroana-*
991 *lytical Chemistry and Interfacial Electrochemistry*, 115(2), 293–308. Retrieved
992 2023-09-28, from [https://www.sciencedirect.com/science/article/pii/](https://www.sciencedirect.com/science/article/pii/S0022072880803330)
993 [S0022072880803330](https://www.sciencedirect.com/science/article/pii/S0022072880803330) doi: 10.1016/S0022-0728(80)80333-0
- 994 Rohatgi, A. (2021). *Webplotdigitizer: Version 4.5*. Retrieved from [https://](https://automeris.io/WebPlotDigitizer)
995 automeris.io/WebPlotDigitizer
- 996 Stack, A. G., & Grantham, M. C. (2010, March). Growth Rate of Calcite Steps As
997 a Function of Aqueous Calcium-to-Carbonate Ratio: Independent Attachment
998 and Detachment of Calcium and Carbonate Ions. *Crystal Growth & Design*,
999 10(3), 1409–1413. Retrieved 2023-09-28, from [https://pubs.acs.org/doi/](https://pubs.acs.org/doi/10.1021/cg901395z)
1000 [10.1021/cg901395z](https://pubs.acs.org/doi/10.1021/cg901395z) doi: 10.1021/cg901395z
- 1001 Subhas, A. V., Adkins, J. F., Rollins, N. E., Naviaux, J., Erez, J., & Berelson,
1002 W. M. (2017, August). Catalysis and chemical mechanisms of calcite dissolu-
1003 tion in seawater. *Proceedings of the National Academy of Sciences*, 114(31),

- 1004 8175–8180. Retrieved 2022-04-26, from [https://www.pnas.org/doi/full/](https://www.pnas.org/doi/full/10.1073/pnas.1703604114)
 1005 10.1073/pnas.1703604114 (Publisher: Proceedings of the National Academy
 1006 of Sciences) doi: 10.1073/pnas.1703604114
- 1007 Subhas, A. V., Dong, S., Naviaux, J. D., Rollins, N. E., Ziveri, P., Gray,
 1008 W., ... Adkins, J. F. (2022). Shallow Calcium Carbonate Cy-
 1009 cling in the North Pacific Ocean. *Global Biogeochemical Cy-*
 1010 *cles*, 36(5), e2022GB007388. Retrieved 2022-06-14, from [http://](http://onlinelibrary.wiley.com/doi/abs/10.1029/2022GB007388)
 1011 onlinelibrary.wiley.com/doi/abs/10.1029/2022GB007388 (_eprint:
 1012 <https://agupubs.onlinelibrary.wiley.com/doi/pdf/10.1029/2022GB007388>) doi:
 1013 10.1029/2022GB007388
- 1014 Subhas, A. V., Rollins, N. E., Berelson, W. M., Dong, S., Erez, J., & Adkins, J. F.
 1015 (2015, December). A novel determination of calcite dissolution kinetics in
 1016 seawater. *Geochimica et Cosmochimica Acta*, 170, 51–68. Retrieved 2022-
 1017 04-26, from [https://www.sciencedirect.com/science/article/pii/](https://www.sciencedirect.com/science/article/pii/S0016703715005050)
 1018 S0016703715005050 doi: 10.1016/j.gca.2015.08.011
- 1019 Sulpis, O., Agrawal, P., Wolthers, M., Munhoven, G., Walker, M., & Middel-
 1020 burg, J. J. (2022, March). Aragonite dissolution protects calcite at the
 1021 seafloor. *Nature Communications*, 13(1), 1104. Retrieved 2022-03-01, from
 1022 <https://www.nature.com/articles/s41467-022-28711-z> (Number: 1
 1023 Publisher: Nature Publishing Group) doi: 10.1038/s41467-022-28711-z
- 1024 Sulpis, O., Jeansson, E., Dinauer, A., Lauvset, S. K., & Middelburg, J. J. (2021,
 1025 June). Calcium carbonate dissolution patterns in the ocean. *Nature Geo-*
 1026 *science*, 14(6), 423–428. Retrieved 2022-02-23, from [https://www.nature](https://www.nature.com/articles/s41561-021-00743-y)
 1027 [.com/articles/s41561-021-00743-y](https://www.nature.com/articles/s41561-021-00743-y) (Number: 6 Publisher: Nature Pub-
 1028 lishing Group) doi: 10.1038/s41561-021-00743-y
- 1029 Sulpis, O., Lauvset, S. K., & Hagens, M. (2020, March). *Current es-*
 1030 *timates of K_{d} and $K_{\text{d}}^{\text{app}}$ appear inconsistent with*
 1031 *measured CO_2 system parameters in cold oceanic re-*
 1032 *gions* (preprint). Data Assimilation/Chemical Tracers/Surface/All Geo-
 1033 graphic Regions. Retrieved 2023-07-06, from [https://os.copernicus.org/](https://os.copernicus.org/preprints/os-2020-19/os-2020-19.pdf)
 1034 [preprints/os-2020-19/os-2020-19.pdf](https://os.copernicus.org/preprints/os-2020-19/os-2020-19.pdf) doi: 10.5194/os-2020-19
- 1035
 1036 Teng, H. H. (2004, January). Controls by saturation state on etch pit formation

- 1037 during calcite dissolution. *Geochimica et Cosmochimica Acta*, 68(2), 253–
1038 262. Retrieved 2022-07-21, from [https://www.sciencedirect.com/science/](https://www.sciencedirect.com/science/article/pii/S001670370300423X)
1039 [article/pii/S001670370300423X](https://www.sciencedirect.com/science/article/pii/S001670370300423X) doi: 10.1016/S0016-7037(03)00423-X
- 1040 Thunell, R. C., Keir, R. S., & Honjo, S. (1981, May). Calcite Dissolution: An
1041 in situ Study in the Panama Basin. *Science*, 212(4495), 659–661. Re-
1042 trieved 2022-03-27, from [https://www.science.org/doi/abs/10.1126/](https://www.science.org/doi/abs/10.1126/science.212.4495.659)
1043 [science.212.4495.659](https://www.science.org/doi/abs/10.1126/science.212.4495.659) (Publisher: American Association for the Advance-
1044 ment of Science) doi: 10.1126/science.212.4495.659
- 1045 Troy, P. J., Li, Y.-H., & Mackenzie, F. T. (1997, March). Changes in Surface Mor-
1046 phology of Calcite Exposed to the Oceanic Water Column. *Aquatic Geochem-*
1047 *istry*, 3(1), 1–20. Retrieved 2022-04-18, from [https://doi.org/10.1023/A:](https://doi.org/10.1023/A:1009652821575)
1048 [1009652821575](https://doi.org/10.1023/A:1009652821575) doi: 10.1023/A:1009652821575
- 1049 Uppström, L. R. (1974, February). The boron/chlorinity ratio of deep-sea
1050 water from the Pacific Ocean. *Deep Sea Research and Oceanographic*
1051 *Abstracts*, 21(2), 161–162. Retrieved 2023-07-06, from [https://www](https://www.sciencedirect.com/science/article/pii/0011747174900746)
1052 [.sciencedirect.com/science/article/pii/0011747174900746](https://www.sciencedirect.com/science/article/pii/0011747174900746) doi:
1053 10.1016/0011-7471(74)90074-6
- 1054 Virtanen, P., Gommers, R., Oliphant, T. E., Haberland, M., Reddy, T., Cour-
1055 napeau, D., ... van Mulbregt, P. (2020, March). SciPy 1.0: fundamen-
1056 tal algorithms for scientific computing in Python. *Nature Methods*, 17(3),
1057 261–272. Retrieved 2023-07-17, from [https://www.nature.com/articles/](https://www.nature.com/articles/s41592-019-0686-2)
1058 [s41592-019-0686-2](https://www.nature.com/articles/s41592-019-0686-2) (Number: 3 Publisher: Nature Publishing Group) doi:
1059 10.1038/s41592-019-0686-2
- 1060 Walter, L. M., & Morse, J. W. (1985, July). The dissolution kinetics of shal-
1061 low marine carbonates in seawater: A laboratory study. *Geochimica*
1062 *et Cosmochimica Acta*, 49(7), 1503–1513. Retrieved 2023-09-27, from
1063 <https://www.sciencedirect.com/science/article/pii/0016703785902558>
1064 doi: 10.1016/0016-7037(85)90255-8
- 1065 Wilson, R. W., Millero, F. J., Taylor, J. R., Walsh, P. J., Christensen, V., Jen-
1066 nings, S., & Grosell, M. (2009). Contribution of Fish to the Marine Inorganic
1067 Carbon Cycle. *Science*, 323(5912), 359–362. Retrieved 2022-06-29, from
1068 <http://www.jstor.org/stable/20402860> (Publisher: American Association
1069 for the Advancement of Science)

- 1070 Wolthers, M., Nehrke, G., Gustafsson, J. P., & Van Cappellen, P. (2012, Jan-
 1071 uary). Calcite growth kinetics: Modeling the effect of solution stoichiom-
 1072 etry. *Geochimica et Cosmochimica Acta*, 77, 121–134. Retrieved 2023-
 1073 05-16, from [https://www.sciencedirect.com/science/article/pii/](https://www.sciencedirect.com/science/article/pii/S0016703711006466)
 1074 S0016703711006466 doi: 10.1016/j.gca.2011.11.003
- 1075 Woosley, R. J., Millero, F. J., & Grosell, M. (2012). The solubility of fish-
 1076 produced high magnesium calcite in seawater. *Journal of Geophys-
 1077 ical Research: Oceans*, 117(C4). Retrieved 2022-06-30, from [https://](https://onlinelibrary.wiley.com/doi/abs/10.1029/2011JC007599)
 1078 onlinelibrary.wiley.com/doi/abs/10.1029/2011JC007599 (_eprint:
 1079 <https://onlinelibrary.wiley.com/doi/pdf/10.1029/2011JC007599>) doi:
 1080 10.1029/2011JC007599
- 1081 Zeebe, R. E., & Wolf-Gladrow, D. (2001). *CO₂ in Seawater: Equilibrium, Kinetics,*
 1082 *Isotopes*. Gulf Professional Publishing. (Google-Books-ID: g3j3Zn4kEscC)
- 1083 Zweng, M., Reagan, J., Seidov, D., Boyer, T., Locarnini, M., Garcia, H., ... Smol-
 1084 yar, I. (2019, January). *World Ocean Atlas 2018, Volume 2: Salinity*. Re-
 1085 trieved 2023-05-16, from <https://archimer.ifremer.fr/doc/00651/76339/>

Supporting Information for ”Synthesis of in situ marine calcium carbonate dissolution kinetic measurements in the water column”

B. A. Cala^{1,2}, O. Sulpis³, M. Wolthers², and M. P. Humphreys¹

¹NIOZ Royal Netherlands Institute for Sea Research, Department of Ocean Systems (OCS), Texel, The Netherlands

²Utrecht University, Department of Earth Sciences, Princetonlaan 8A, 3584 CB Utrecht, The Netherlands

³CEREGE, Aix Marseille Univ, CNRS, IRD, INRAE, Aix-en-Provence, France

Contents of this file

1. Text S1 to S7
2. Figures S1 to S17
3. Tables S1 to S2

Introduction

This document contains supporting information and figures for the main text. In particular, we validate the our approach to estimate Ω and compare our results to those of the CDisK-IV cruise. We also provide several other figures relevant to the discussion in the main text.

Text S1: Method validation

CANYON-B was validated against 20% of GLODAPv2 data that was not used for training the model and additionally on data from GO-SHIP cruises that have not been included in GLODAPv2 training data (Bittig et al., 2018).

We used more recent GLODAP bottle data to re-evaluate the method's performance in accurately estimating environmental variables and carbonate system parameters. CANYON-B was trained on GLODAPv2 data (Olsen et al., 2016), therefore the validation dataset consists of cruises that were added since then in GLODAPv2.2022 (Lauvset et al., 2022). However, it is important to note that data from new cruises added to successive GLODAP versions are still assessed and, if necessary, adjusted for consistency with the existing GLODAP dataset before being added to each new version, so they are not truly independent. We therefore excluded any datasets that had received adjustments from the validation. Only stations with a maximum sample depth of at least 1000 m were included, because most in situ experiments were conducted deeper in the water column and we didn't want to focus on surface measurements for the validation. Data from the Sea of Japan was excluded because CANYON-B performed significantly worse there (Figure S1) and none of the dissolution experiments took place in or near that particular region (Figure S2). Overall, the validation dataset contained 31670 data points. When only data points below 1000 m depth were considered, the validation set still contained 14536 data points. Following the method described earlier (Section 2.2), hydrographic variables were predicted with WOA18 and CANYON-B only based on the geographic location, depth season, and year of the measurement.

Evaluation of all estimated variables from WOA18 and CANYON-B was performed using three metrics: mean absolute error (MAE), root mean squared error (RMSE), and R-squared (R^2). Additionally, Ω was calculated using all three possible parameter pair combinations of TA, DC and pH to assess whether one pair performed significantly better or worse.

The results are shown in Table S1. Over the entire dataset, the MAE for $\Omega_{DIC,pH}$ is 0.11 and the RMSE is 0.21. However, the method performs much better below 1000 m with an MAE of 0.02 and an RMSE of 0.03. The errors are mainly at the surface, where the WOA18 climatology cannot capture the natural (e.g., seasonal) variation of temperature, salinity, and dissolved oxygen in time and space. Here, the RMSE for the CANYON-B output is much larger than the uncertainty of CANYON-B (Bittig et al., 2018). Below 1000 m, where over 85% of dissolution measurements were made, the errors are much more acceptable and for the carbonate system parameters comparable to the estimates of inter-cruise consistency in GLODAP ($4 \mu\text{mol kg}^{-1}$ for TA and DIC, and 0.01 for pH) (Lauvset et al., 2022).

The choice of parameter pair affects the calculated Ω value, as discussed by Patsavas, Byrne, Wanninkhof, Feely, and Cai (2015) and Naviaux et al. (2019). Using the (TA, DIC) pair results in higher saturation states than (TA, pH) or (DIC, pH). Naviaux et al. (2019) found that $\Omega_{TA,pH}$ explains the occurrence of dissolution better than $\Omega_{TA,DIC}$. Using the (TA, DIC) pair instead of (DIC, pH) results on average in 6% higher Ω_{ca} . The offset between (TA, pH) and (DIC, pH) is much smaller, with a difference of 0.4% (Figure S6). We therefore decided to use the (DIC, pH) pair as it was very consistent with (TA, pH), which was recommended by Naviaux et al. (2019), but has the advantage

that $[\text{CO}_3^{2-}]$ and therefore Ω calculated from DIC and pH is independent both of the nutrient values and of all the other non-carbonate components of TA (Humphreys et al., 2022) and therefore would not be influenced by any missing terms in the TA equation or biases in non-carbonate equilibrium constants and total salt concentrations.

Text S2: Expocodes of considered cruises

All considered: 49NZ20170208, 29HE20190406, 45CE20170427, 49UF20170110, 49UF20170228, 49UF20170408, 49UF20170502, 49UF20170612, 49UF20170719, 49UF20180129, 49UF20180406, 49UF20180518, 49UF20180709, 49UP20170107, 49UP20170201, 49UP20170425, 49UP20170623, 49UP20170815, 49UP20171125, 49UP20180110, 49UP20180228, 49UP20180501, 49UP20180614, 740H20180228, 91AA20171209, 18DD20170205, 18DD20170604, 18DD20190205, 18DD20190602, 320620170703, 320620170820, 325020190403, 33RO20180423, 49NZ20191229, 58JH20190515, 74JC20181103, 33HQ20170826, 33HQ20180807, 33HQ20190806, 33RO20170718, 49NZ20191205, 49UF20190207, 49UF20190716, 49UF20200108, 49UF20200201, 49UF20200605, 49UF20200619, 49UF20200730, 49UF20210202, 49UF20210407, 49UF20210515, 49UP20181206, 49UP20190110, 49UP20190228, 49UP20190408, 49UP20190516, 49UP20190612, 49UP20190811, 49UP20191125, 49UP20200227, 49UP20200605, 49UP20200730, 49UP20201019, 49UP20210113, 49UP20210301, 49UP20210425

Excluded (Sea of Japan): 49UF20171107, 49UF20180927, 49UF20190916, 49UF20201021

Excluded because of adjusted values: 33RO20161119, 096U20180111, 320620180309, 18DL20200722

Text S3: Comparison to CDisK-IV measurements

Figure S9 shows the comparison of the Ω values obtained through estimates of other hydrographic variables, as described in Section 2.2 with the Ω calculated from real cruise measurements (Berelson et al., 2022). While the method estimates Ω well at depths below approximately 500 m, at shallower depths the method can overestimate Ω by up to 0.25 which is larger than the uncertainty assigned to Ω . The CDisK-IV dataset does not include the uncertainty for Ω . This was calculated by propagating the uncertainties given in Naviaux et al. (2019) in PyCO2SYS. The resulting uncertainty for Ω are so small that they are not visible in the plot.

In Figure S10 it becomes clear that the problem lies mainly with the estimation of pH in CANYON-B. Temperature and Salinity are captured well in the estimates, and so is TA. pH appears to be overestimated by CANYON-B. This dataset does not include measured dissolved oxygen concentrations to evaluate whether that is the cause of the apparent overestimation of pH in CANYON-B. However, using CTD bottle data (Dong et al., 2022) from the same cruise and stations and comparing those to the values interpolated from WOA18 following the method described in Section 2.2, we see that oxygen concentration is indeed overestimated (Figure S11c). Higher dissolved oxygen is generally linked to greater primary productivity and/or lower remineralisation, both of which processes that raise pH, presumably leading CANYON-B to give a higher pH estimate.

Text S4: Are the experiment conditions representative of the open ocean?

Figure S12 shows that the chemical/physical environments where dissolution experiments have been conducted, capture a wide range of marine environments. The main

regions that are underrepresented are temperatures above 8°C , which occur in the shallow ocean where seawater is usually oversaturated with respect to calcite, and DIC values less than $2100\mu\text{mol kg}^{-1}$.

Text S5: Uncertainty of Ω

The uncertainty of Ω decreases exponentially with depth (Figure S13). These results are comparable to the RMSE values obtained during the validation of the method in Text S1. In the upper hundreds of meters, there are large fluctuations in temperature, salinity, and dissolved oxygen with time which increase the uncertainty of Ω . For most of the samples, the uncertainty is less than 0.05 for Ω at depths below the saturation horizons. The absolute uncertainty for Ω is higher in Atlantic (experiments M77, HE78). However, Ω there is usually higher than in the Pacific and overall the relative uncertainties are the same in both ocean basins.

Text S6: Multiple Linear Regression

We attempted to predict the dissolution rate with multiple linear regression (MLR), using the same predictors as in the XGBoost method. We performed MLR with Ordinary Least Squares (OLS) using the statsmodels package (version 0.13.5) for Python. The fit of the model was assessed with adjusted R^2 which adjusts for the number of predictors used in the model. An adjusted R^2 of only 0.247 was achieved, meaning that the model did not account for around 75% of the variance in the data.

While linear regressions are often preferred due to their straightforward interpretability, they cannot capture non-linear and complex relationships between the predictors and the dependent variables which are likely to occur in the real world. This is the case here and

therefore a supervised machine learning approach is used for our analysis described here in the main paper.

Text S7: Hyperparameters for the XGBoost Regressor

n_estimators: 70

max_depth: 6

min_child_weight: 6

colsample_bytree: 0.75

gamma: 0

learning_rate: 0.11

reg_alpha: 1

reg_lambda: 10

References

- Berelson, W. M., Adkins, J. F., Subhas, A. V., Dong, S., & Naviaux, J. D. (2022, August). *In situ experimentally determined dissolution rates of biogenic calcites along a North Pacific transect between Hawaii and Alaska (KM1712 expedition) in August 2017*. Biological and Chemical Oceanography Data Management Office (BCO-DMO). Retrieved 2023-07-04, from <https://hdl.handle.net/1912/29186> doi: 10.26008/1912/BCO-DMO.856409.2
- Bittig, H. C., Steinhoff, T., Claustre, H., Fiedler, B., Williams, N. L., Sauzède, R., ... Gattuso, J.-P. (2018). An Alternative to Static Climatologies: Robust Estimation of Open Ocean CO₂ Variables and Nutrient Concentrations From T, S, and O₂ Data

- Using Bayesian Neural Networks. *Frontiers in Marine Science*, 5. Retrieved 2022-03-03, from <https://www.frontiersin.org/article/10.3389/fmars.2018.00328>
- Dong, S., Liu, X., Naviaux, J. D., Subhas, A. V., Rollins, N. E., Adkins, J. F., & Berelson, W. M. (2022, February). *Carbonate chemistry and CTD data collected along a North Pacific transect between Hawaii and Alaska on R/V Kilo Moana cruise KM1712 in August 2017*. Biological and Chemical Oceanography Data Management Office (BCO-DMO). Retrieved 2023-10-11, from <https://hdl.handle.net/1912/27970> doi: 10.26008/1912/BCO-DMO.836954.2
- Humphreys, M. P., Lewis, E. R., Sharp, J. D., & Pierrot, D. (2022, January). PyCO2SYS v1.8: marine carbonate system calculations in Python. *Geoscientific Model Development*, 15(1), 15–43. Retrieved 2023-06-29, from <https://gmd.copernicus.org/articles/15/15/2022/> (Publisher: Copernicus GmbH) doi: 10.5194/gmd-15-15-2022
- Lauvset, S. K., Lange, N., Tanhua, T., Bittig, H. C., Olsen, A., Kozyr, A., ... Key, R. M. (2022, December). GLODAPv2.2022: the latest version of the global interior ocean biogeochemical data product. *Earth System Science Data*, 14(12), 5543–5572. Retrieved 2023-06-29, from <https://essd.copernicus.org/articles/14/5543/2022/> (Publisher: Copernicus GmbH) doi: 10.5194/essd-14-5543-2022
- Naviaux, J. D., Subhas, A. V., Dong, S., Rollins, N. E., Liu, X., Byrne, R. H., ... Adkins, J. F. (2019, September). Calcite dissolution rates in seawater: Lab vs. in-situ measurements and inhibition by organic matter. *Marine Chemistry*, 215, 103684. Retrieved 2022-04-01, from <https://www.sciencedirect.com/science/article/pii/S0304420319300763> doi: 10.1016/j.marchem.2019.103684

- Olsen, A., Key, R. M., van Heuven, S., Lauvset, S. K., Velo, A., Lin, X., . . . Suzuki, T. (2016, August). The Global Ocean Data Analysis Project version 2 (GLODAPv2) – an internally consistent data product for the world ocean. *Earth System Science Data*, 8(2), 297–323. Retrieved 2023-06-29, from <https://essd.copernicus.org/articles/8/297/2016/> (Publisher: Copernicus GmbH) doi: 10.5194/essd-8-297-2016
- Patsavas, M. C., Byrne, R. H., Wanninkhof, R., Feely, R. A., & Cai, W.-J. (2015, November). Internal consistency of marine carbonate system measurements and assessments of aragonite saturation state: Insights from two U.S. coastal cruises. *Marine Chemistry*, 176, 9–20. Retrieved 2023-07-11, from <https://www.sciencedirect.com/science/article/pii/S0304420315300074> doi: 10.1016/j.marchem.2015.06.022

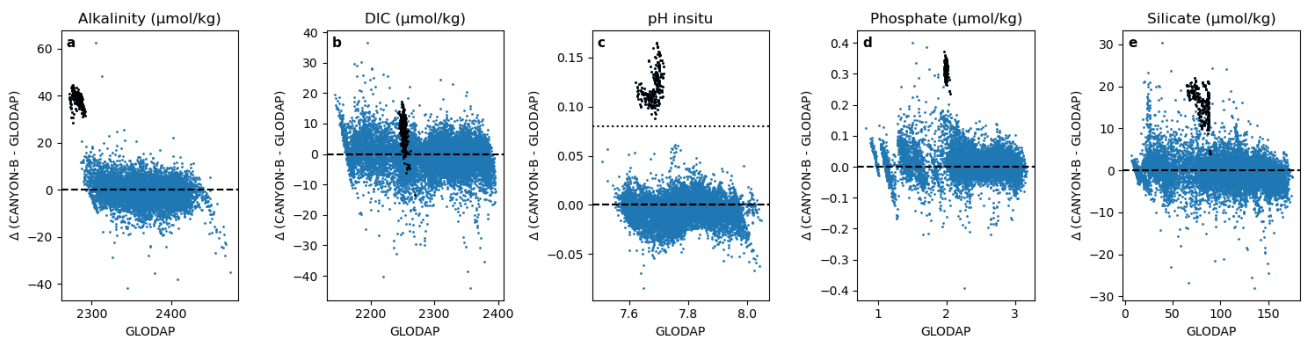


Figure S1. Comparison of (a) TA, (b) DIC, (c) pH, and (d) phosphate, (e) silicate data obtained through the method using WOA18 and CANYON-B to the GLODAPv2.2022 validation set. This figure also shows that CANYON-B performs significantly worse the subset of the data in the Sea of Japan (marked black; above the dotted line at 0.08 in (c)). Those stations were subsequently excluded from the validation set.

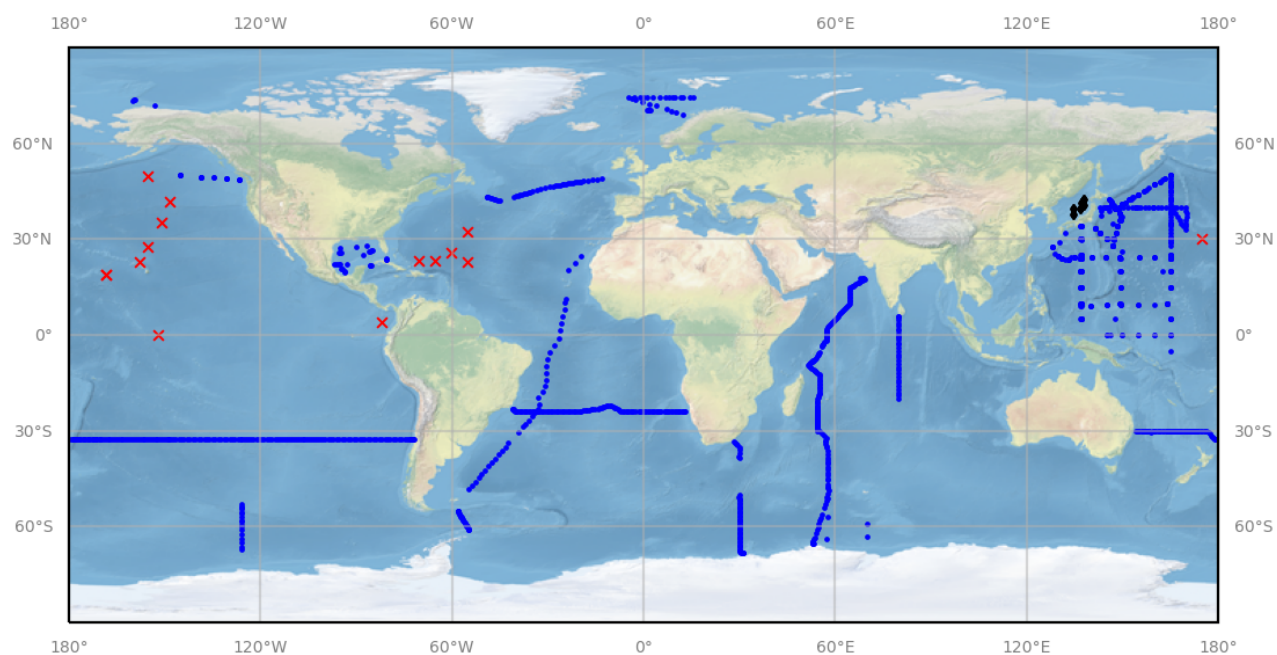


Figure S2. Stations of the validation set (blue) which is bottle data from GLODAPv2.2022 cruises after 2016 (excluding adjusted cruises). Also shown are the stations in the Sea of Japan that were excluded from the validation set (black) and the sites of the dissolution experiments (red crosses).

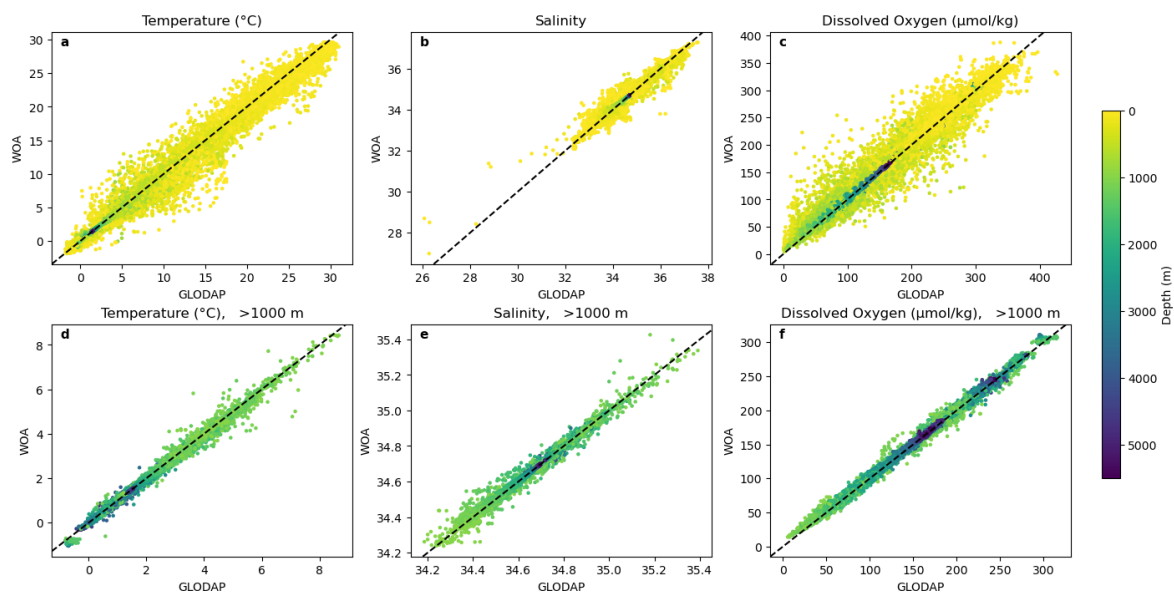


Figure S3. Comparison of the obtained WOA18 data to the GLODAP validation set, showing (a),(d) temperature, (b),(e) salinity and (c),(f) dissolved oxygen concentration. The top row shows all data, while the bottom row only shows data from deeper than 1000 m.

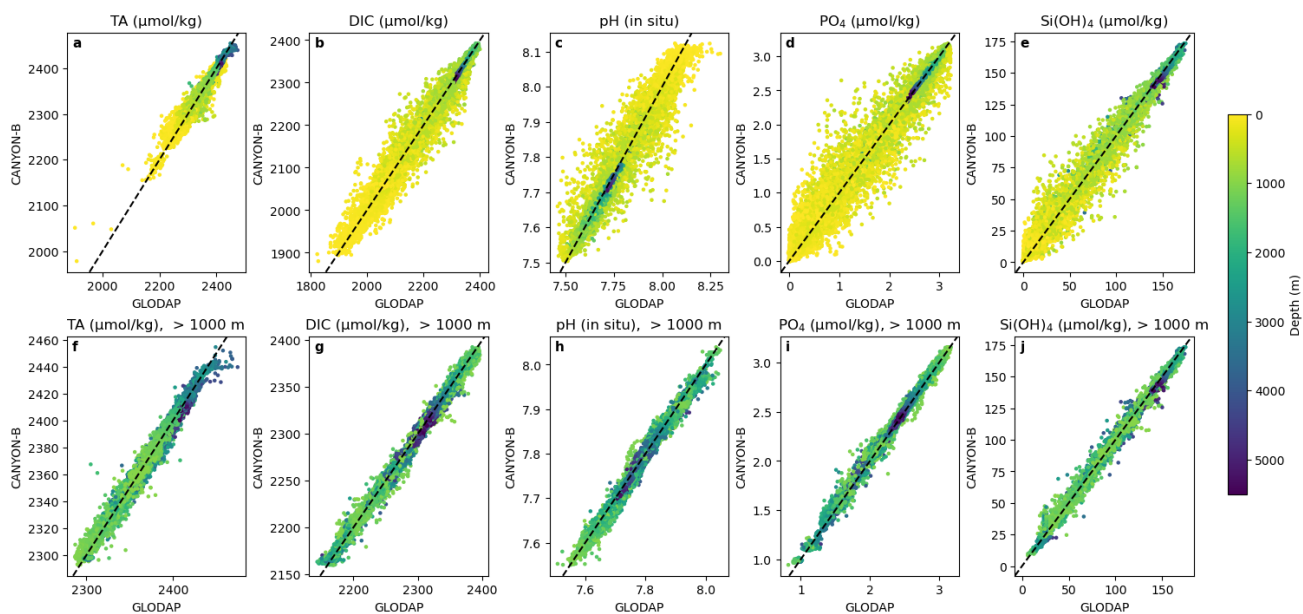


Figure S4. Comparison of the obtained CANYON-B data to the GLODAP validation set, showing (a),(f) TA, (b),(g) DIC, (c),(h) in situ pH, (d),(i) phosphate concentration and (e),(j) silicate concentration. The bottom row only shows data points below 1000 m depth.

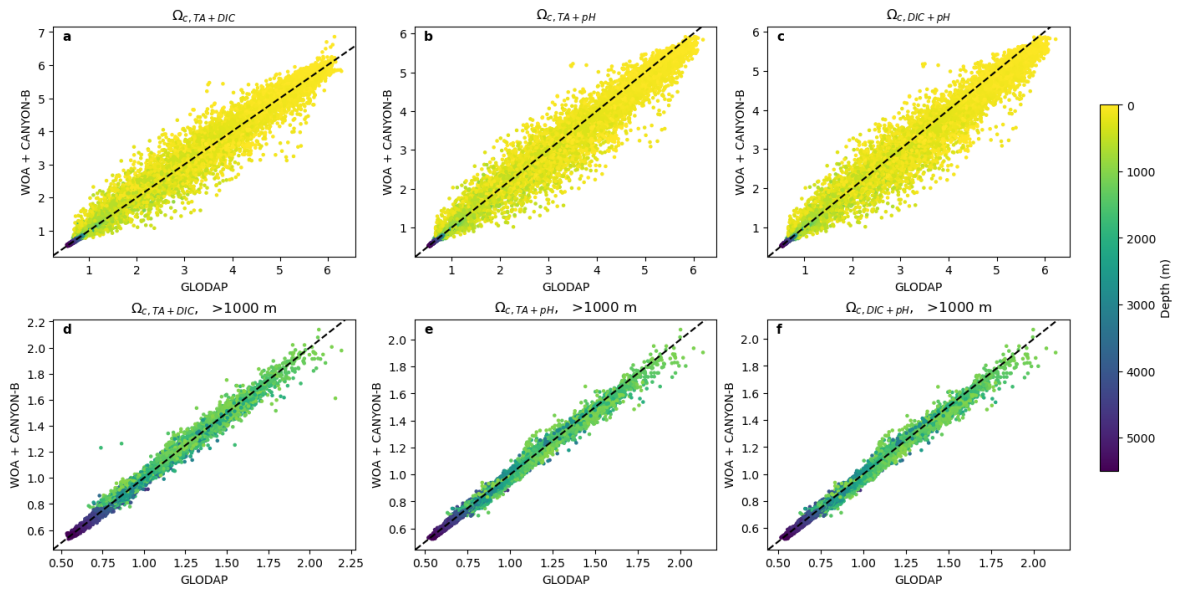


Figure S5. Comparison of Ω the obtained CANYON-B data to the GLODAP validation set, using the (a),(d) TA-DIC (b),(e) TA-pH, and (c),(f) DIC-pH parameter pair. The top row shows all data, while the bottom row only shows data from deeper than 1000 m.

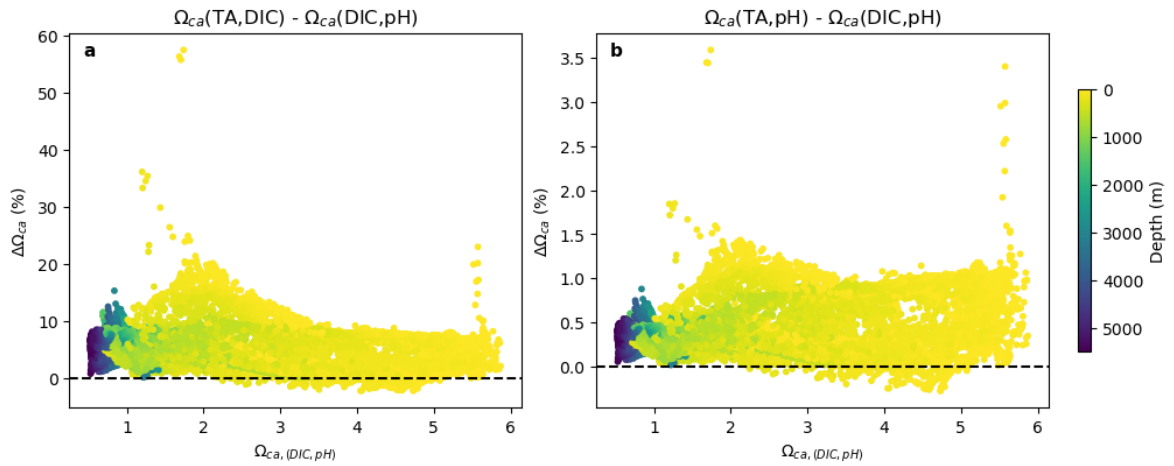


Figure S6. Relative offset of Ω_{ca} depending on which parameter pair was used to calculate it. Difference between (a) TA-DIC and DIC-pH and (b) TA-pH and DIC-pH are shown. Note the difference in scale on the y-axis.

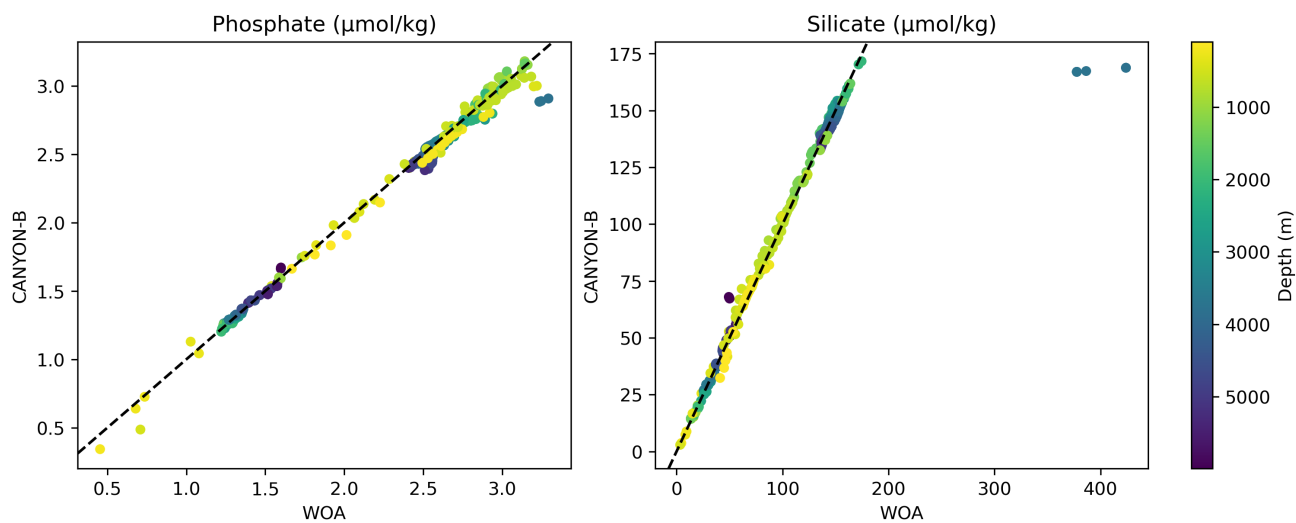


Figure S7. Comparison of (a) phosphate and (b) silicate concentration interpolated from the WOA18 dataset as described in Section 2.2 and from CANYON-B.

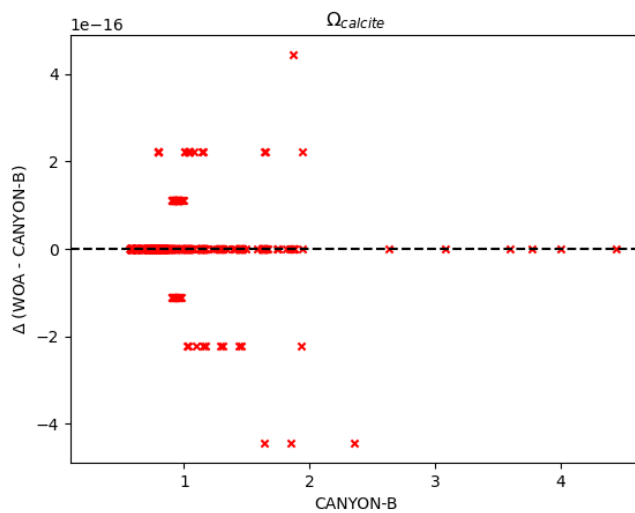


Figure S8. Difference in Ω , depending on whether the nutrients used to calculate Ω stem from WOA18 or CANYON-B.

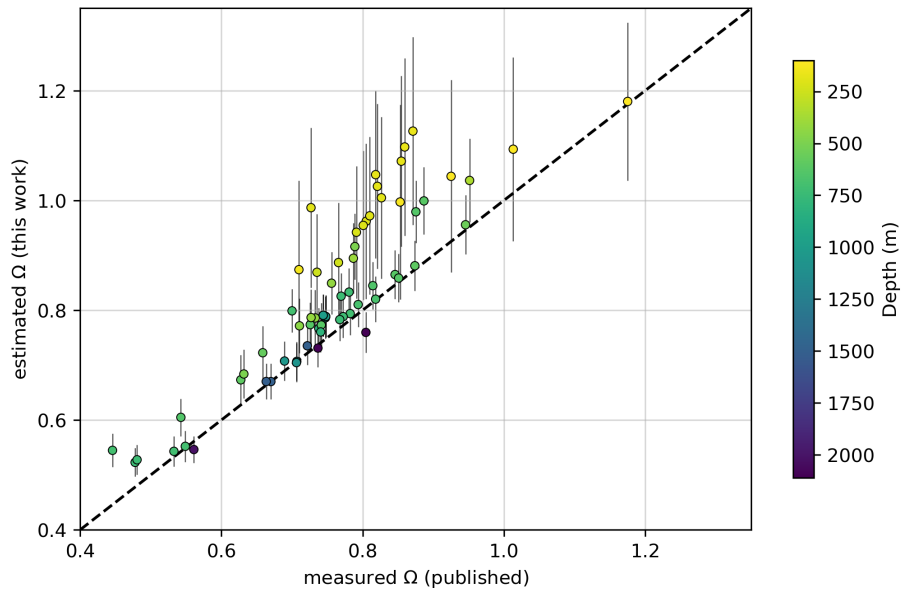


Figure S9. Comparison of Ω estimated through the method using WOA18 and CANYON-B to the values that were calculated using TA and pH values measured at the dissolution experiment on the CDisK-IV cruise (described by (Naviaux et al., 2019)).

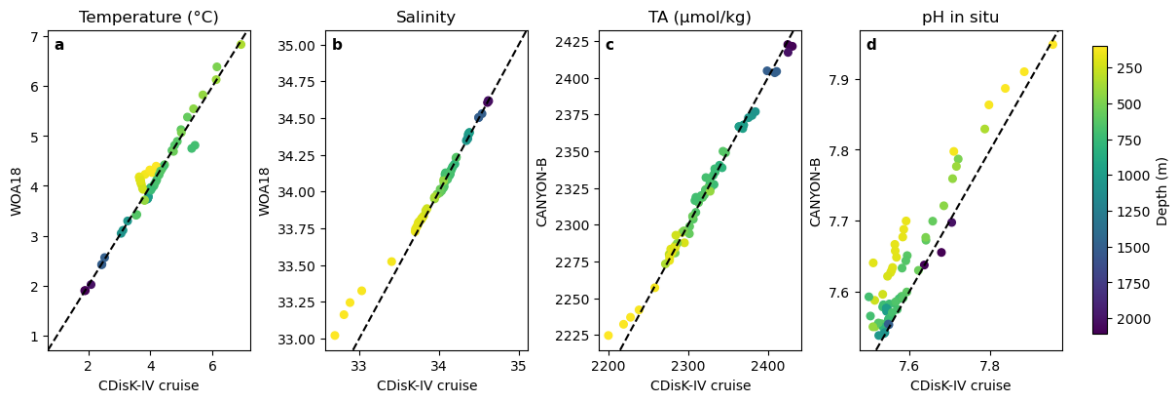


Figure S10. Comparison of (a) temperature, (b) salinity, (c) TA, and (d) pH (in situ) obtained through the method using WOA18 and CANYON-B to the CDisK-IV cruise measurements for the dissolution experiments.

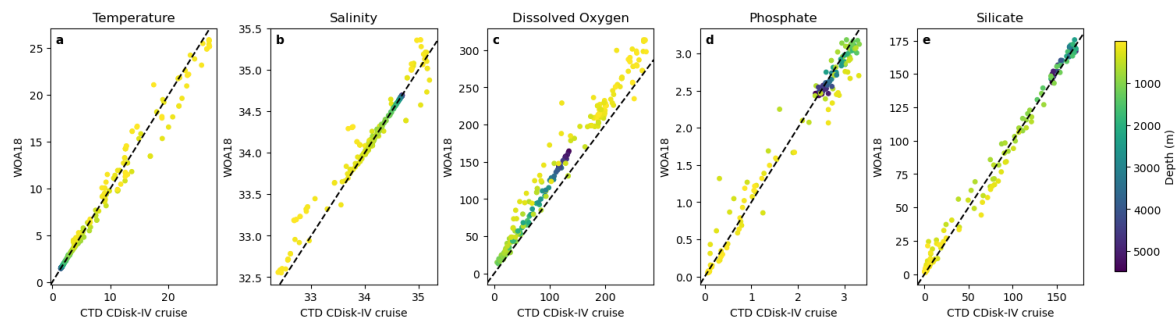


Figure S11. Comparison of (a) temperature, (b) salinity, (c) dissolved oxygen, (d) phosphate and (e) silicate concentration obtained from WOA18 to the CDisK-IV CTD bottle data.

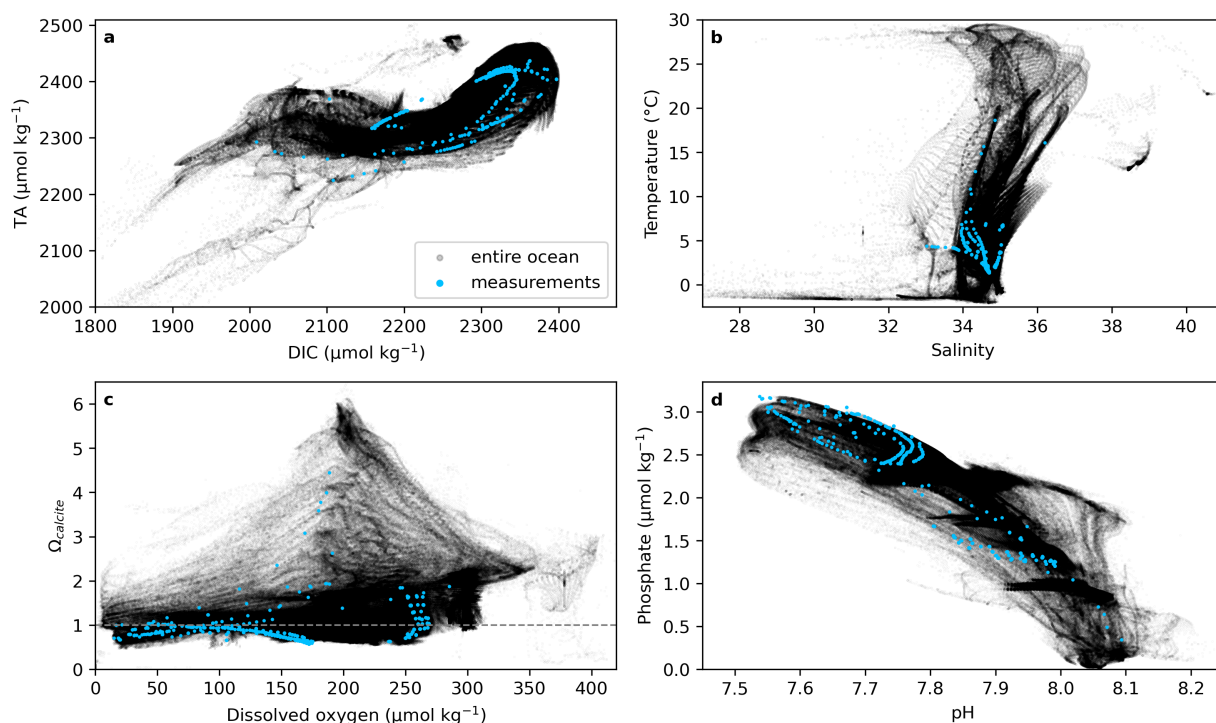


Figure S12. Environmental variables of the locations where in situ measurements were conducted plotted on top of the WOA18 field and the carbonate parameters derived from that field with CANYON-B to assess how representative the dissolution experiments are. (a) TA against DIC, (b) Temperature against Salinity, (c) Ω_{ca} against dissolved oxygen concentration, and (d) phosphate concentration against in situ pH

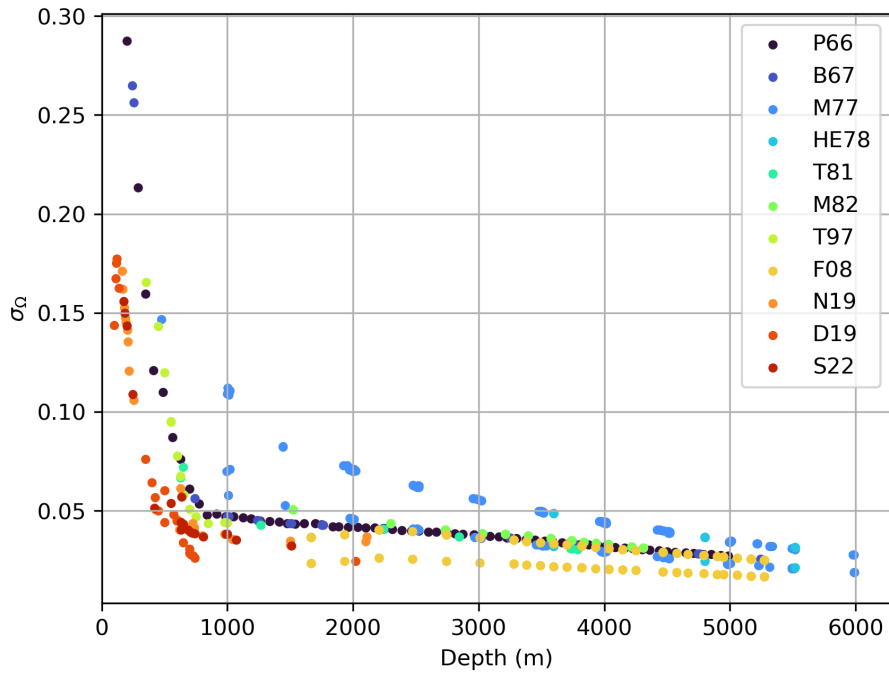


Figure S13. Uncertainty of Ω with depth for the different studies, assessed as described in Section 2.3.

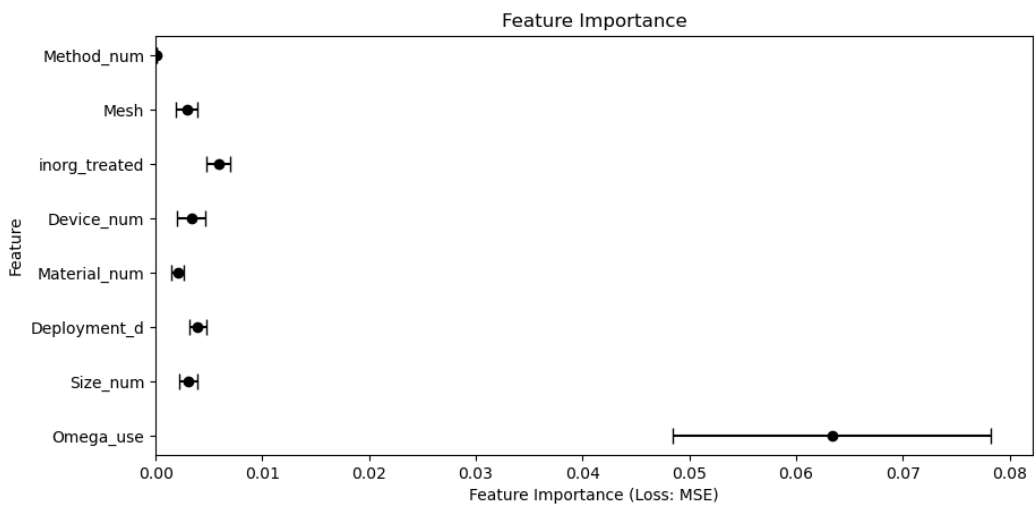


Figure S14. Permutation Feature Importance for the prediction of dissolution rates. The greater the increase of the model’s prediction error if a feature is not contributing to the prediction, the larger that feature’s importance. The scoring metric here is MSE (the average increase is plotted with the standard deviations).

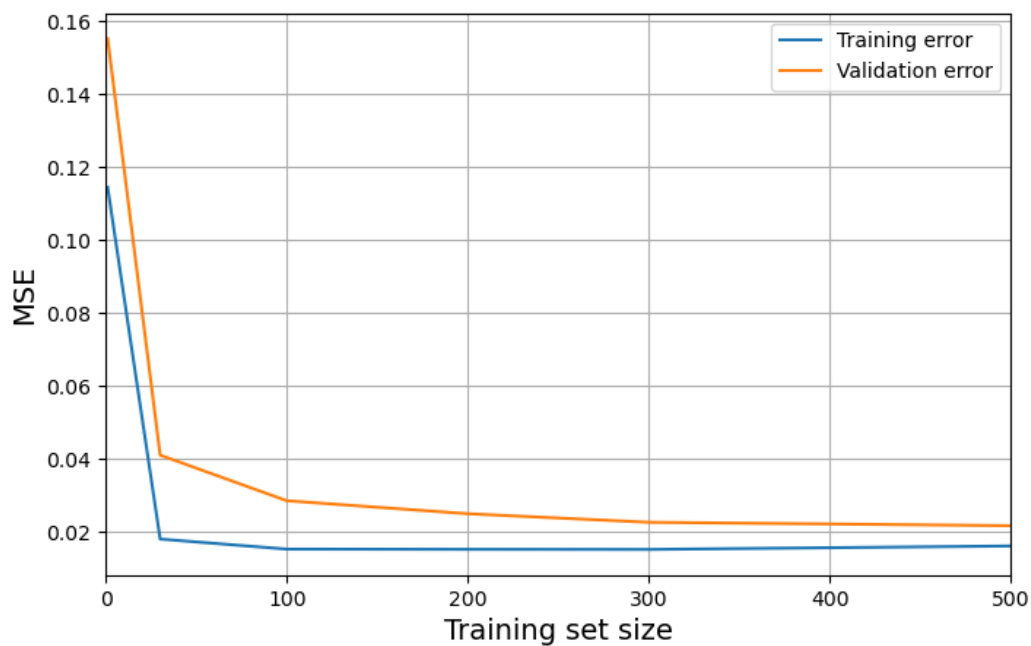


Figure S15. Learning curve for trained XGBoost model with MSE as scoring metric.

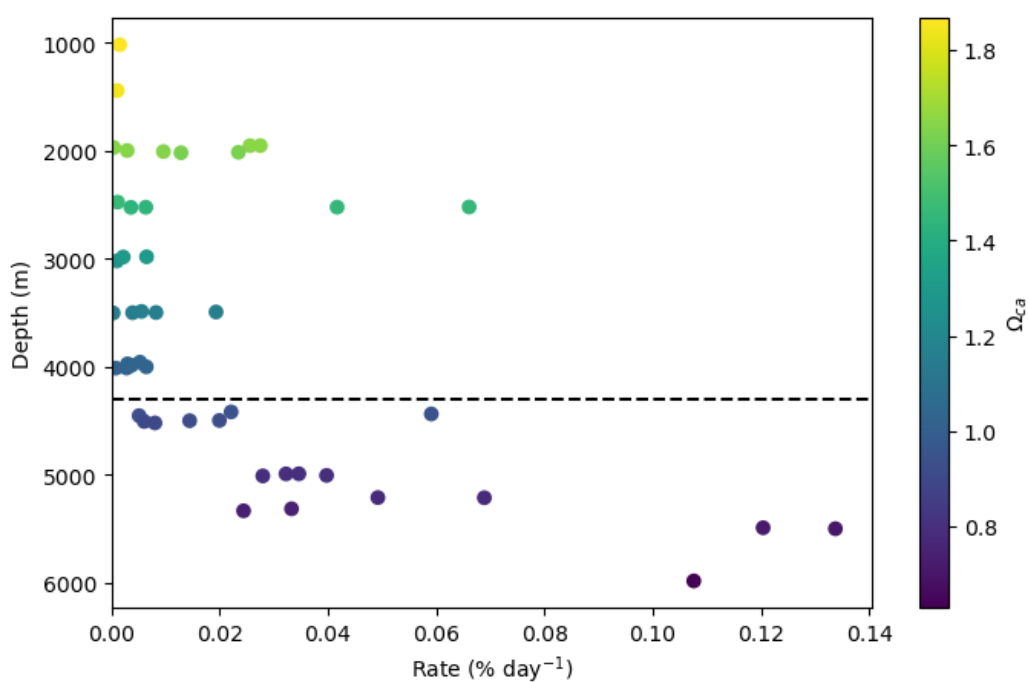


Figure S16. Dissolution rate of calcite as a function of depth for all 4 stations in M77. The approximate location of the saturation horizon is shown as a dashed line. Significant dissolution is observed at 2000 and 2500 m.

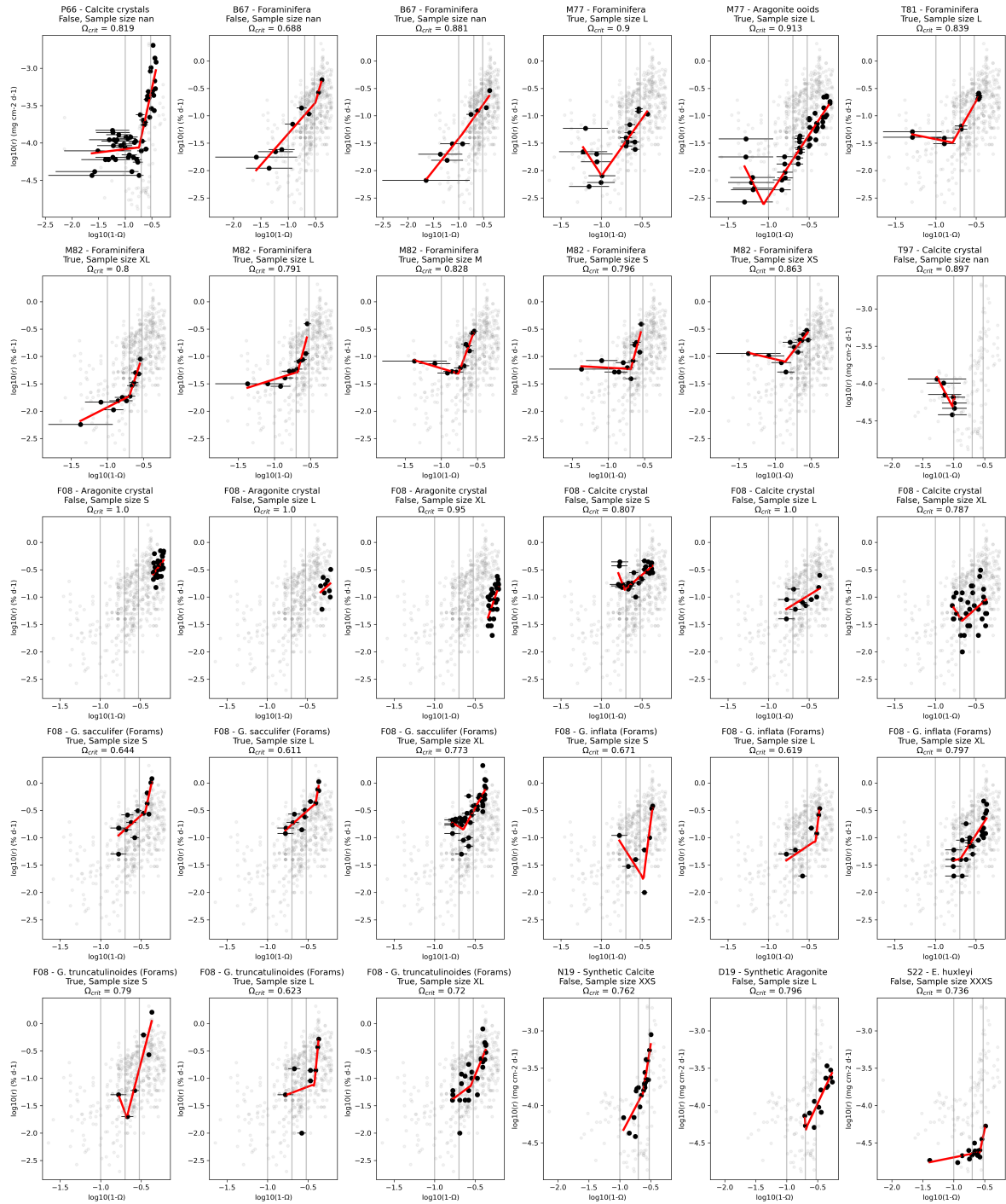


Figure S17. Ω_{crit} for dissolution rates determined with the Error Function (Equation 8). Each panel shows a different sample set. Each study was further divided by sample material, whether organic coatings were left intact and the size of the sample, as indicated by the text above each panel. The grey vertical lines mark the saturation state at $\Omega = 0.9, 0.8,$ and 0.7 from left to right. Grey data points are other data points in the data compilation that were not part of this study. The Ω_{crit} values producing the best fit are shown in red above each panel. $\Omega_{crit} = 1$ or negative values mean that the best fit is produced if only one dissolution regime with no Ω_{crit} is assumed.

Table S1. Performance of WOA + CANYON-B method, compared against bottle data in the GLODAPv2.2022 data set that were not used to train or test CANYON-B (not part of GLODAPv2) and excluding data from the Sea of Japan as well as already adjusted data sets.

| | | complete dataset | | | >1000 m depth | | |
|---------------------------|------------------------------------|------------------|-------|------|---------------|------|------|
| | | MAE | RMSE | R2 | MAE | RMSE | R2 |
| WOA18 | Temperature ($^{\circ}\text{C}$) | 0.48 | 0.98 | 0.98 | 0.06 | 0.12 | 0.99 |
| | Salinity | 0.06 | 0.13 | 0.94 | 0.01 | 0.01 | 0.99 |
| | Doxy ($\mu\text{mol kg}^{-1}$) | 7.50 | 13.64 | 0.96 | 3.00 | 4.36 | 0.99 |
| CANYON-B | TA ($\mu\text{mol kg}^{-1}$) | 5.03 | 7.78 | 0.98 | 3.17 | 4.32 | 0.99 |
| | DIC ($\mu\text{mol kg}^{-1}$) | 8.91 | 15.18 | 0.98 | 3.59 | 4.96 | 0.99 |
| | pH (in situ) | 0.02 | 0.03 | 0.96 | 0.01 | 0.01 | 0.98 |
| | PO4 ($\mu\text{mol kg}^{-1}$) | 0.07 | 0.14 | 0.98 | 0.03 | 0.04 | 0.99 |
| | SiOH4 ($\mu\text{mol kg}^{-1}$) | 2.83 | 4.94 | 0.99 | 2.32 | 3.25 | 0.99 |
| Ω_{calcite} | $\Omega_{\text{TA,DIC}}$ | 0.10 | 0.20 | 0.98 | 0.02 | 0.03 | 0.99 |
| | $\Omega_{\text{TA,pH}}$ | 0.11 | 0.21 | 0.98 | 0.02 | 0.03 | 0.99 |
| | $\Omega_{\text{DIC,pH}}$ | 0.11 | 0.21 | 0.98 | 0.02 | 0.03 | 0.99 |

Table S2. Size fractions of samples.

| Size category | XXXS | XXS | XS | S | M | L | XL | XXL |
|---------------------------------|------|---------|----------|-----------|-----------|-----------|------|---------------------|
| Size fraction (μm) | <10 | 10 - 53 | 62 - 125 | 125 - 177 | 177 - 250 | 250 - 420 | >420 | 700 - 1000, >831 |
| # of samples | 21 | 32 | 13 | 96 | 16 | 261 | 182 | 6 |